

## Nobeyama Inward-motion Survey toward SCUBA-2 Cores in Orion

KEN'ICHI TATEMATSU,<sup>1,2</sup> YOU-TING YEH,<sup>3</sup> NAOMI HIRANO,<sup>3</sup> SHENG-YUAN LIU,<sup>3</sup> TIE LIU,<sup>4,5,6</sup> GWANJEONG KIM,<sup>1</sup>  
SOMNATH DUTTA,<sup>3</sup> DIPEN SAHU,<sup>3</sup> HEE-WEON YI,<sup>7,8</sup> JEONG-EUN LEE,<sup>8</sup> CHIN-FEI LEE,<sup>3</sup> SHIH-YING HSU,<sup>9,3</sup> YUEFANG WU,<sup>10</sup>  
KEE-TAE KIM,<sup>7,11</sup> JAMES DI FRANCESCO,<sup>12,13</sup> MIKA JUVELA,<sup>14</sup> L. VIKTOR TÓTH,<sup>15</sup> NEAL J. EVANS II,<sup>16</sup> MINHO CHOI,<sup>5</sup>  
MIJU KANG,<sup>5</sup> MARK A. THOMPSON,<sup>17,18</sup> GARY A. FULLER,<sup>19</sup> DI LI,<sup>20</sup> PATRICIO SANHUEZA,<sup>21,2</sup> KE WANG,<sup>22,23</sup>  
DAVID EDEN,<sup>24</sup> TAKESHI SAKAI,<sup>25</sup> RYO KANDORI,<sup>26</sup> CHAU-CHING CHIONG,<sup>3</sup> SHANGHUO LI,<sup>5,4,27,28</sup> ET AL., AND  
JCMT LARGE PROGRAM “SCOPE” COLLABORATION

<sup>1</sup>Nobeyama Radio Observatory, National Astronomical Observatory of Japan, National Institutes of Natural Sciences, Nobeyama,  
Minamimaki, Minamisaku, Nagano 384-1305, Japan

<sup>2</sup>Department of Astronomical Science, The Graduate University for Advanced Studies, SOKENDAI, 2-21-1 Osawa, Mitaka, Tokyo  
181-8588, Japan

<sup>3</sup>Academia Sinica Institute of Astronomy and Astrophysics, 11F of Astronomy-Mathematics Building, AS/NTU. No.1, Sec. 4, Roosevelt  
Rd, Taipei 10617, Taiwan, R.O.C.

<sup>4</sup>Shanghai Astronomical Observatory, Chinese Academy of Sciences, 80 Nandan Road, Shanghai 200030, P. R. China

<sup>5</sup>Korea Astronomy and Space Science Institute, 776 Daedeok-daero, Yuseong-gu, Daejeon 34055, South Korea

<sup>6</sup>East Asian Observatory, 660 N. A'ohoku Place, Hilo, HI 96720, USA

<sup>7</sup>Korea Astronomy and Space Science Institute, 776 Daedeok-daero, Yuseong-gu, Daejeon 34055, Republic of Korea

<sup>8</sup>School of Space Research, Kyung Hee University, Seochon-Dong, Giheung-Gu, Yongin-Si, Gyeonggi-Do, 446-701, Republic of Korea

<sup>9</sup>National Taiwan University, No. 1, Sec. 4, Roosevelt Rd., Taipei 10617, Taiwan, R.O.C.

<sup>10</sup>Department of Astronomy, Peking University, 100871, Beijing, China

<sup>11</sup>University of Science and Technology, Korea (UST), 217 Gajeong-ro, Yuseong-gu, Daejeon 34113, Republic of Korea

<sup>12</sup>Herzberg Astronomy & Astrophysics, National Research Council of Canada, 5071 West Saanich Road, Victoria, BC V9E 2E7, Canada

<sup>13</sup>Department of Physics and Astronomy, University of Victoria, Victoria, BC V8W 2Y2, Canada

<sup>14</sup>Department of Physics, P.O. Box 64, FI-00014, University of Helsinki, Finland

<sup>15</sup>Department of Astronomy, Eötvös Loránd University, Pázmány Péter sétány 1/A, H-1117 Budapest, Hungary

<sup>16</sup>Department of Astronomy, The University of Texas at Austin, 2515 Speedway, Stop C1400, Austin, TX 78712–1205, USA

<sup>17</sup>School of Physics & Astronomy, University of Leeds, Leeds, LS2 9JT, UK

<sup>18</sup>Centre for Astrophysics Research, Science & Technology Research Institute, University of Hertfordshire, Hatfield, AL10 9AB, UK

<sup>19</sup>Jodrell Bank Centre for Astrophysics, School of Physics and Astronomy, University of Manchester, Oxford Road, Manchester, M13  
9PL, UK

<sup>20</sup>National Astronomical Observatories, Chinese Academy of Sciences, Beijing, 100012, China

<sup>21</sup>National Astronomical Observatory of Japan, National Institutes of Natural Sciences, 2-21-1 Osawa, Mitaka, Tokyo 181-8588, Japan

<sup>22</sup>The Kavli Institute for Astronomy and Astrophysics, Peking University, 5 Yiheyuan Road, Haidian District, Beijing 100871, P. R.  
China

<sup>23</sup>European Southern Observatory, Karl-Schwarzschild-Str. 2 D-85748 Garching bei München, Germany

<sup>24</sup>Astrophysics Research Institute, Liverpool John Moores University, IC2, Liverpool Science Park, 146 Brownlow Hill, Liverpool L3 5RF,  
UK

<sup>25</sup>Graduate School of Informatics and Engineering, The University of Electro-Communications, Chofu, Tokyo 182-8585, Japan

<sup>26</sup>Astrobiology Center of NINS, 2-21-1 Osawa, Mitaka, Tokyo 181-8588, Japan

<sup>27</sup>Center for Astrophysics — Harvard & Smithsonian, 60 Garden Street, Cambridge, MA 02138, USA

<sup>28</sup>University of Chinese Academy of Sciences, 19A Yuquanlu, Beijing 100049, P. R. China

## ABSTRACT

We surveyed 36 SCUBA-2 cores (30 starless and 6 protostellar) identified by submillimeter continuum emission in Orion, including ALMASOP cores, to search for inward motions. We used the Nobeyama 45 m radio telescope, and mapped the cores in the  $J = 1 \rightarrow 0$  transitions of  $\text{HCO}^+$ ,  $\text{H}^{13}\text{CO}^+$ ,  $\text{N}_2\text{H}^+$ , HNC, and  $\text{HN}^{13}\text{C}$ . The asymmetry parameter (normalized velocity difference)  $\Delta V$ , which is the ratio of the velocity difference between  $\text{HCO}^+$  and  $\text{H}^{13}\text{CO}^+$  to the  $\text{H}^{13}\text{CO}^+$  line width is biased toward

negative values, suggesting that inward motions are more dominant than outward motions. Three starless cores (10%) are identified as cores having blue-skewed line profiles, and another three starless cores (10%) are identified as possibly blue-skewed line profiles. All of them are associated with cores with  $\text{H}^{13}\text{CO}^+$  emission. The peak velocity difference between  $\text{HCO}^+$  and  $\text{H}^{13}\text{CO}^+$  up to  $0.9 \text{ km s}^{-1}$ , suggesting that some of inward motions exceeds the sound speed for the quiescent gas ( $\sim 10 \text{ K}$ ). The mean of  $\Delta V$  of the six cores above was derived to be  $-1.4 \pm 0.7$ . Although the sample number is small, there is no clear indication that inward motions are observed predominantly at the latest stage in the starless phase, judging from the Chemical Evolution Factor version 2.0 (CEF2.0) of Kim et al. One core, G211.16–19.33North3 also observed with ALMA ACA in  $\text{DCO}^+ J = 3 \rightarrow 2$  shows blue-skewed features. Velocity offset in the blue-skewed line profile with a dip in the  $\text{DCO}^+ J = 3 \rightarrow 2$  line is larger ( $\sim 0.5 \text{ km s}^{-1}$ ) than that in  $\text{HCO}^+ J = 1 \rightarrow 0$  ( $\sim 0.2 \text{ km s}^{-1}$ ), which may represent gravitational acceleration of inward motions.

*Keywords:* Uni ed Astronomy Thesaurus concepts: Early-type stars (430), Star forming regions (1565), Star formation (1569), Interstellar medium (847), Interstellar line emission (844)

## 1. INTRODUCTION

We wonder how star formation starts. It is suggested that denser cores have shorter lifetimes in units of the free-fall time; the lifetime of a core with an  $\text{H}_2$  density of  $10^4 \text{ cm}^{-3}$  is approximately  $10^6 \text{ yr}$ , which is longer than the free-fall time ( $t_{ff} = 3 \times 10^5 \text{ yr}$ ), whereas that of a core with an  $\text{H}_2$  density of  $10^6 \text{ cm}^{-3}$  seems close to the free-fall time ( $t_{ff} = 3 \times 10^4 \text{ yr}$ ) (Jessop & Ward-Thompson 2000; André et al. 2014; Könyves et al. 2015; Tokuda et al. 2020). Here, the lifetime is estimated from the fraction of cores that contain protostars or YSOs. Starless cores with an  $\text{H}_2$  density of  $10^{4-5} \text{ cm}^{-3}$  seem not to be dynamically collapsing, and then they may be close to dynamically stable equilibrium. If such stable cores finally form stars, there will be a mechanism to make them unstable. Mass inflow onto cores is one of the candidate mechanisms (Gómez et al. 2007). If inward motions do occur, we wonder whether it does at free-fall or slower. In addition, we wonder when starless cores start dynamical inward motions. Given that there is a stage of a (quasi)static molecular cloud core before star formation, the flow of the ambient matter onto a core, which may make a core unstable, and collapse within the core, which will form a protostar or protostars. L1544 provided us with the first example of the latter case in the starless phase (Tafalla et al. 1998). For terminology, we adopt that of (Padoan et al. 2020), i.e., inward motions on scales of 1–10 pc (filaments to cores), 0.01–0.1 pc (cores to disks), and 100–1000 au (disks to stars) as inflow, infall, and accretion, respectively.

How can we estimate the evolutionary stage of a core? Tatematsu et al. (2017) and Kim et al. (2020) developed the Chemical Evolution Factor (CEF), a measure for the starless core on the basis of logarithmic deuterium fraction of  $\text{N}_2\text{D}^+$  and DNC. Another tracer of starless core evolution is the distribution of density. The ALMA ACA is sensitive to a concentration of gas near the core center. Tokuda et al. (2020) used detectability in the dust continuum emission with the ALMA ACA; detection of a  $\sim 10''$  (0.02 pc at  $\sim 150 \text{ pc}$  distance) sized dense-gas structure with densities of  $\gtrsim 8 \times 10^5 \text{ cm}^{-3}$  is supposed to represent later stages in the starless core phase. Sahu et al. (2021) reported the detection of five centrally concentrated dense structures with sizes of  $\sim 2000 \text{ au}$  using the ALMA 12 m Array ( $\sim 300 \text{ au}$  resolution), which most likely represent the latest stages of starless cores. It would be fruitful to investigate when inward motions occur. Flows of matter onto cores along and/or across filaments are also of our interest (Hacar & Tafalla 2011; Friesen et al. 2013; Palmeirim et al. 2013; Lu et al. 2018; Chen et al. 2020; Sanhueza et al. 2021).

There are surveys in various star forming regions for inward motions, which include Wang et al. (1995), Mardones et al. (1997), Lee et al. (1999), Gregersen et al. (2000a), Gregersen et al. (2000b), Fuller et al. (2005), Velusamy et al. (2008), Contreras et al. (2018), Jackson et al. (2019), and Yi et al. (2021). A popular way is to search for the blue-skewed line profile with a dip in optically thick lines such as  $\text{HCO}^+$ . Gregersen et al. (2000a), who made an inward-motion survey using  $\text{HCO}^+ J = 3 \rightarrow 2$ , concluded “making an unambiguous claim for infall is somewhat difficult.” Clear cases of the signature of infall in terms of redshifted absorption include Evans et al. (2015) and Olguin et al. (2021) observed with the ALMA. We need to investigate from various aspects whether observed profiles truly represent inward motions or not. In addition, we should note that the gas with inward motions may not show its signature in observations.

We select cores in the Orion molecular clouds which were previously observed with the ALMA in the ALMASOP collaboration (Dutta et al. 2020) and/or with the Nobeyama 45 m telescope (Kim et al. 2020; Tatematsu et al. 2021).

These cores were originally taken from the catalog of SCUBA-2 cores inside Planck Galactic Cold Clumps (PGCCs) in Orion compiled by Yi et al. (2018). All SCUBA-2 cores identified in PGCCs in the SCOPE collaboration is cataloged in Eden et al. (2019). Temperatures of PGCCs range from 10 to 17 K. Please refer to Planck Collaboration et al. (2011) and ? for PGCCs. SCUBA-2 cores in Orion have similar distances ( $420 \pm 40$  pc, Kounkel et al. (2017); Getman et al. (2019)) so that we can avoid distance-dependent effects such as different beam dilution (Kim et al. 2020). Prior to our study, Velusamy et al. (2008) surveyed inward motions toward starless cores in Orion, but actually the samples do not have overlapping except for one core. They surveyed two regions in the Orion A cloud, whereas we selected only cores in cold clumps identified as PGCCs but in wider Orion areas containing the  $\lambda$  Ori, Orion A and B regions. In addition, at that time, the information on young stellar objects (YSOs) was limited. Now, more sensitive YSO information such as Furlan et al. (2016) is available. For example, HOPS-10, -11, -12, -89, and -92 are associated with cores studied by Velusamy et al. (2008) which were regarded as starless. Yi et al. (2021) surveyed inward motions in HCO ( $J = 1 \rightarrow 0$ ) with KVN 21m telescope (30'' beam) toward 80 cores (55 starless and 25 protostellar) of the 119 SCUBA-2 cores in Orion by Yi et al. (2018). Our observations have a 1.8 times better spatial resolution. We will go back to their work later.

## 2. OBSERVATIONS

We carried out mapping observations of 33 fields containing 36 SCUBA-2 cores using the 45 m radio telescope of the Nobeyama Radio Observatory<sup>1</sup> (CG201001; P.I. = Gwanjeong Kim). Table 1 summarizes the numbers of clumps and cores in related studies. The observed lines and their rest frequencies are listed in Table 2. The critical and effective densities are adopted from Shirley et al. (2015). Observations were conducted from 2020 December to 2021 February. For the receiver frontend, the FOur-beam REceiver System on the 45 m Telescope (FOREST; Minamidani et al. 2016) was employed for simultaneous observations of four lines. HCO<sup>+</sup>, H<sup>13</sup>CO<sup>+</sup>, HNC, and HN<sup>13</sup>C were observed simultaneously. The half-power beam width (HPBW) and main-beam efficiency  $\eta_{mb}$  at 86 GHz were  $18''.2 \pm 0''.3$  (0.037 pc at 420 pc distance) and  $50.4\% \pm 3.2\%$ , respectively. For the receiver backend, the Spectral Analysis Machine for the 45 m telescope (SAM45; Kamazaki et al. 2012) was employed with a spectral resolution of 30.52 kHz, which corresponds to  $\sim 0.1$  km s<sup>-1</sup> at 82 GHz. The precise value of the velocity resolution is given in Table 2.

The On-the-Fly (OTF) mapping observations (Sawada et al. 2008) of the 33 fields were in most cases performed in the R.A. and Decl. directions to minimize striping effects. However, 30% of the observations were made only in one direction. The map size was  $3' \times 3'$ . Three neighboring cores (cores 6, 12, and 21) were mapped simultaneously with cores 5, 11, and 20, respectively. The JCMT SCUBA-2 core names and their coordinates are summarized in Table 3. The association with YSOs is taken from Kim et al. (2020), who observed with the Nobeyama 45 m telescope. 30 cores out of the 36 observed cores are known to be starless, while the remaining six cores are protostellar. However, identification of either starless or protostellar depends on observational spatial resolutions. These six protostellar cores are classified as starless with offset YSOs by Dutta et al. (2020) with the ALMA ACA at a spatial resolution of  $7''.6 \times 4''.1$ . The core names, radius, and mass of SCUBA-2 cores are taken from Yi et al. (2018). We converted the FWHM (full width at half maximum) diameter of Yi et al. (2018) to the HWHM (half width at half maximum) radius  $R$  by dividing by two. The position switching mode was employed, and the reference positions were ( $\Delta$ R.A.,  $\Delta$ Decl.) = ( $-30', 0'$ ), ( $20', 20'$ ), ( $-20', -20'$ ), and ( $20', 20'$ ) from the map center, for cores 1–12, 13–16, 17–18, and 19–36, respectively. It took approximately 3 hours to achieve an rms noise level of 0.1 K for a  $3' \times 3'$  map. The typical system temperature was 200 K. The telescope pointing calibration was performed at 1.0–1.5 hours intervals toward the SiO maser source, Orion KL, which resulted in a pointing accuracy of  $\lesssim 5''$ .

Linear baselines were subtracted from the spectral data, and the data were stacked on a grid of  $6''$  with the Bessel-Gauss function on the NOSTAR program of the Nobeyama Radio Observatory (Sawada et al. 2008). The R.A. and Decl. scan data were basket-weaved through the method of Emerson & Graeve (1988). The line intensity was expressed in terms of the antenna temperature  $T_A^*$  corrected for atmospheric extinction using the standard chopper wheel calibration.

We also used the N<sub>2</sub>H<sup>+</sup> data of our previous observations reported in Tatematsu et al. (2021) in this analysis, to avoid redundant N<sub>2</sub>H<sup>+</sup> observations. In addition, we adopted the SCUBA-2 core properties, HWHM radius and density, from Yi et al. (2018) (Table. They adopted distances of 380 pc and 420 pc for the  $\lambda$  Ori region and the Ori

<sup>1</sup> Nobeyama Radio Observatory is a branch of the National Astronomical Observatory of Japan, National Institutes of Natural Sciences.

**Table 1.** Clump and Core Samples

Category	Clump Number	Core Number	Reference
PGCC	13188	. . .	Planck Collaboration et al. (2016)
SCUBA-2 core in PGCC (SCOPE)	558	3528	Eden et al. (2019)
SCUBA-2 core in Orion	40	119	Yi et al. (2018)
starless SCUBA-2 core in Orion studied here	. . .	30	this work

A and B region taken from Perryman et al. (1997) and a combination of Jeffries (2007) and Sandstrom et al. (2007), respectively, and we simply adopted their physical parameter based on them.

### 3. RESULTS

#### 3.1. Infall Velocity and the Asymmetry Parameter

We search for observational evidence of inward motions. The double-peaked profile due to absorption by foreground lower excitation-temperature gas is called “self-reversal” (Loren 1976; Blitz & Thaddeus 1980). The “self-reversal” profile contains a dip (suppression) between two emission peaks. If the cloud or cloud core has a systematic motion with respect to the core center such as collapse and expansion, the line profile of an optically thick line with an absorption dip will have asymmetry in shape. Cases of the collapse are explained by Zhou (1992) and Zhou et al. (1993) in detail. In such cases, we will see blue-skewed line profiles with dips, whose lower-velocity (blue) peaks are brighter than its higher-velocity (red) peaks. Starless cores are likely to have kinetic-temperature gradients decreasing inward toward the core center (Evans et al. 2001), but if the radial density gradient decreasing outward is steep enough, cores may have excitation-temperature gradients decreasing outward, which will cause self-reversal or blue-skewed line profiles with dips.

Table 4 summarizes the peak intensities and peak velocities of the molecular lines toward the SCUBA-2 core centers. The peak is determined from the spectrum without any fitting, so the nominal peak velocity accuracy is equal to the spectral resolution ( $0.1 \text{ km s}^{-1}$ ). Differences between the line velocities help us to identify possible inward motions. Table 6 summarizes velocity differences. The  $\text{HCO}^+$  line is often optically thick, judged from a comparison with the  $\text{H}^{13}\text{CO}^+$  emission in intensity and line shape, and is thought to represent gas motions in the line shape such as line profile asymmetry (Gegersen et al. 2000a,b; Fuller et al. 2005; Velusamy et al. 2008; Jackson et al. 2019). The  $\text{H}^{13}\text{CO}^+$  line is optically thinner than  $\text{HCO}^+$ , and the velocity difference between the  $\text{HCO}^+$  and  $\text{H}^{13}\text{CO}^+$  peak velocities might reflect whether the gas may move inward or outward, if the sign of the velocity difference is negative or positive, respectively. As an independent measure, we also use velocity differences between  $\text{HCO}^+$  and  $\text{N}_2\text{H}^+$ . The  $\text{N}_2\text{H}^+$  line emission is optically thinner than  $\text{HCO}^+$ . It has hyperfine splitting (Caselli et al. 1995), and we adopted the isolated hyperfine component ( $F_1, F = 0, 1 \rightarrow 1, 2$ ) to avoid overlapping with neighboring components. We take the difference in the line peak velocity, as a measure of the inward velocity (Table 6). The velocity difference ranges up to  $0.9 \text{ km s}^{-1}$ . Lee et al. (1999) concluded that inward motions in low-mass starless cores are subsonic, which is different from our conclusion. It is possible that all the observed velocity shifts may not represent the velocity field of a single core. We investigate each case later. Fuller et al. (2005) studied cores associated with candidate high-mass protostars, and obtained large values of inward motions of  $0.1\text{--}1 \text{ km s}^{-1}$ . We compare radius and mass of these samples. The HWHM radius and mass of our Orion cores, which is located in an intermediate-mass star forming region, are  $0.015\text{--}1.125 \text{ pc}$  (with a mean of  $0.083 \text{ pc}$  and a median of  $0.050 \text{ pc}$ ) and  $0.15\text{--}7.1 M_\odot$  (with a mean of  $1.8 M_\odot$  and a median of  $1.2 M_\odot$ ), respectively. Caselli et al. (1995), Lee et al. (1999), and Gegersen et al. (2000b) studies cores in low-mass star forming regions, and some of them were observed by Kirk et al. (2005). The HWHM radius and mass of these cores are  $0.008\text{--}0.37 \text{ pc}$  (with a mean of  $0.020 \text{ pc}$  and a median of  $0.020 \text{ pc}$ ) and  $0.20\text{--}1.6 M_\odot$  (with a mean of  $0.55 M_\odot$  and a median of  $0.35 M_\odot$ ), respectively. Then, our Orion cores are larger and more massive than their dark cloud cores. Most of the cores in high-mass star forming regions studied by Fuller et al. (2005) are distributed in a range of  $0\text{--}100 M_\odot$  with a distribution tail to even higher mass, and so they are more massive than our Orion cores.

**Table 2.** Observed Lines

Line	Frequency GHz	Frequency Reference	Velocity Resolution km s <sup>-1</sup>	Upper Energy Level $E_u$ K	Critical Density at 10 K cm <sup>-3</sup>	Effective Density at 10 K cm <sup>-3</sup>
HCO <sup>+</sup> $J = 1 \rightarrow 0$	89.1885230	Pickett et al. (1998)	0.103	4.3	$6.8 \times 10^4$	$9.5 \times 10^2$
H <sup>13</sup> CO <sup>+</sup> $J = 1 \rightarrow 0$	86.7542884	Pickett et al. (1998)	0.105	4.2	$6.2 \times 10^4$	$3.9 \times 10^4$
HNC $J = 1 \rightarrow 0$	90.6635930	Pickett et al. (1998)	0.101	4.4	$1.4 \times 10^5$	$1.0 \times 10^4$
HN <sup>13</sup> C $J = 1 \rightarrow 0$	87.0908500	Pickett et al. (1998)	0.105	4.2	...	...
N <sub>2</sub> H <sup>+</sup> $J = 1 \rightarrow 0$	93.1737767	Caselli et al. (1995)	0.098	4.5	$6.1 \times 10^4$	$6.8 \times 10^4$

**Table 3.** Name, Coordinates, SCUBA-2 Radius, and Mass of the SCUBA-2 Core

Core Number	JCMT Core Name	R.A. (J2000)	Decl. (J2000)	YSO Ass.	ALMA Source Name	$R$	$M$
		h m s	° ' "			pc	$M_{\odot}$
1	G191.90–11.21North	5 31 28.99	12 58 55.0	starless	"G191.90–11.21N "	0.050	$0.34 \pm 0.07$
2	G198.69–09.12North1	5 52 29.61	8 15 37.0	starless	G198.69–09.12N1	0.045	$0.43 \pm 0.07$
3	G198.69–09.12North2	5 52 25.30	8 15 8.8	starless	G198.69–09.12N2	0.030	$0.21 \pm 0.02$
4	G201.72–11.22	5 50 54.53	4 37 42.6	starless	. . .	1.125	$1.83 \pm 0.21$
5	G203.21–11.20East2	5 53 47.90	3 23 8.9	starless	G203.21–11.20E2	0.060	$2.65 \pm 1.73$
6	G203.21–11.20East1	5 53 51.11	3 23 4.9	starless	G203.21–11.20E1	0.060	$2.50 \pm 0.43$
7	G205.46–14.56North1	5 46 5.49	0 9 32.4	starless	G205.46–14.56M3	0.015	$0.39 \pm 0.06$
8	G206.21–16.17North	5 41 39.28	-1 35 52.9	starless	G206.21–16.17N	0.105	$4.97 \pm 0.05$
9	G206.21–16.17South	5 41 34.23	-1 37 28.8	starless	G206.21–16.17S	0.055	$1.05 \pm 0.46$
10	G206.93–16.61East1	5 41 40.54	-2 17 4.3	starless	G206.93–16.61E1	0.060	$5.37 \pm 0.54$
11	G206.93–16.61West4	5 41 25.84	-2 19 28.4	starless	. . .	0.040	$1.25 \pm 0.67$
12	G206.93–16.61West5	5 41 28.77	-2 20 4.3	starless	G206.93–16.61W4	0.055	$7.10 \pm 0.72$
13	G207.36–19.82North2	5 30 50.67	-4 10 15.6	protostellar	G207.36–19.82N2	0.020	$0.44 \pm 0.14$
14	G207.36–19.82North4	5 30 44.81	-4 10 27.6	starless	G207.36–19.82N4	0.015	$0.15 \pm 0.05$
15	G207.36–19.82South	5 30 46.81	-4 12 29.4	starless	G207.36–19.82S	0.095	$2.01 \pm 0.91$
16	G208.68–19.20North2	5 35 20.45	-5 0 53.0	protostellar	G208.68–19.20N2	0.025	$2.22 \pm 1.15$
17	G209.05–19.73North	5 34 3.96	-5 32 42.5	starless	. . .	0.115	$2.83 \pm 0.15$
18	G209.05–19.73South	5 34 3.12	-5 34 11.0	starless	. . .	0.070	$1.65 \pm 0.29$
19	G209.29–19.65North1	5 35 0.25	-5 40 2.4	starless	G209.29–19.65N1	0.035	$0.70 \pm 0.10$
20	G209.29–19.65South1	5 34 55.99	-5 46 3.2	starless	G209.29–19.65S1	0.035	$1.49 \pm 0.26$
21	G209.29–19.65South2	5 34 53.81	-5 46 12.8	starless	G209.29–19.65S2	0.040	$2.31 \pm 0.97$
22	G209.55–19.68North2	5 35 7.01	-5 56 38.4	starless	G209.55–19.68N2	0.025	$0.28 \pm 0.07$
23	G209.77–19.40West	5 36 21.19	-6 1 32.7	starless	G209.77–19.40W	0.045	$0.50 \pm 0.07$
24	G209.77–19.40East2	5 36 32.19	-6 2 4.7	starless	G209.77–19.40E2	0.035	$1.20 \pm 0.56$
25	G209.77–19.40East3	5 36 35.94	-6 2 44.7	starless	G209.77–19.40E3	0.020	$0.26 \pm 0.12$
26	G209.94–19.52North	5 36 11.55	-6 10 44.8	protostellar	G209.94–19.52N	0.065	$2.81 \pm 0.28$
27	G209.79–19.80West	5 35 11.19	-6 14 0.7	starless	G209.79–19.80W	0.135	$7.06 \pm 2.56$
28	G209.94–19.52South1	5 36 24.96	-6 14 4.7	starless	G209.94–19.52S1	0.080	$3.52 \pm 0.09$
29	G210.37–19.53North	5 36 55.03	-6 34 33.2	starless	G210.37–19.53N	0.030	$0.28 \pm 0.02$
30	G210.82–19.47North2	5 37 59.84	-6 57 9.9	starless	G210.82–19.47N2	0.030	$0.15 \pm 0.05$
31	G211.16–19.33North5	5 38 46.00	-7 10 41.9	protostellar	G211.16–19.33N5	0.060	$0.64 \pm 0.18$
32	G211.16–19.33North3	5 39 2.26	-7 11 7.9	starless	G211.16–19.33N3	0.050	$0.41 \pm 0.12$
33	G211.16–19.33North4	5 38 55.67	-7 11 25.9	protostellar	G211.16–19.33N4	0.065	$0.51 \pm 0.04$
34	G211.72–19.25South1	5 40 19.04	-7 34 28.8	starless	G211.72–19.25S1	0.060	$1.15 \pm 0.82$
35	G212.10–19.15North1	5 41 21.56	-7 52 27.7	protostellar	G212.10–19.15N1	0.090	$3.52 \pm 1.68$
36	G215.44–16.38	5 56 58.45	-9 32 42.3	starless	G215.44–16.38	0.030	$0.19 \pm 0.04$

185 Note that we need to take into account various aspects to judge if they mean inward or outward motions. Some  
 186 cores may be oscillating (Lada et al. 2003; Aguti et al. 2007), although our spatial resolution with respect to the core  
 187 size will be insufficient to identify it. We adopt the asymmetry parameter  $\delta V$  (Mardones et al. 1997), which is the  
 188 velocity difference between optically thicker and thinner lines, normalized to the FWHM line width of an optically  
 189 thinner line. They regard significant detection if the absolute value of the asymmetry parameter exceeds their criterion  
 190 of 0.25. We define our asymmetry parameter as  $\delta V = [v(\text{HCO}^+) - v(\text{H}^{13}\text{CO}^+)] / \Delta v(\text{H}^{13}\text{CO}^+)$ , and listed it in Table  
 191 6. Note that, we eliminated protostellar cores in the column of  $\delta V$ . The number in parentheses indicates that



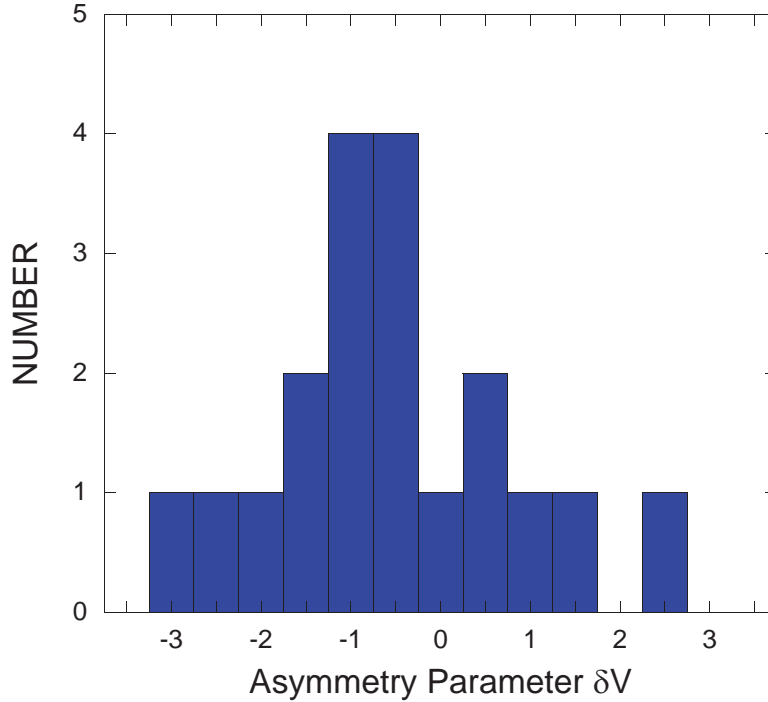


**Figure 1.** Histogram of the asymmetry parameter (line velocity difference normalized to the  $\text{H}^{13}\text{CO}^+$  FWHM line width)  $\delta V$  between  $\text{HCO}^+$  and  $\text{H}^{13}\text{CO}^+$  for the starless cores. Here, we do not include cores which show multiple velocity components in  $\text{H}^{13}\text{CO}^+$  ( $\delta V$  in parentheses in Table 6).

multiple velocity components are observed in  $\text{H}^{13}\text{CO}^+$ . The error in  $\delta V$  will mainly come from the velocity difference  $[v(\text{HCO}^+) - v(\text{H}^{13}\text{CO}^+)]$ . The uncertainty in  $\delta V$  will be about 30%, taking into account the nominal velocity resolution ( $0.1 \text{ km s}^{-1}$ ), the effect of the S/N ratio on accuracy in the velocity difference, and the accuracy in velocity in  $\text{H}^{13}\text{CO}^+$  Gaussian fitting ( $< 0.1 \text{ km s}^{-1}$ ), and typical  $\text{H}^{13}\text{CO}^+$  linewidth. However, it should be noted that the existence of multiple velocity components may affect the velocity difference. Table 5 list the number of velocity components observed in  $\text{H}^{13}\text{CO}$  and  $\text{N}_2\text{H}^+$  ( $F_1, F = 0, 1 \rightarrow 1, 2$ ). Later, we investigate the molecular line spectra to see the effect of multiple velocity components. The absolute values of our asymmetry parameters ranging up to 3.2 are much larger in general in the absolute value than those in [Mardones et al. \(1997\)](#), who studied low-mass molecular cloud cores containing candidate protostars at a convolved spatial resolution of  $37''$  ( $0.027 \text{ pc}$  at  $150 \text{ pc}$  distance) to alleviate different beam sizes of the employed telescopes. Their maximum absolute value was 1.16. [Gregersen et al. \(2000b\)](#) studied starless cores at a spatial resolution of  $26''$  ( $0.019 \text{ pc}$  at  $150 \text{ pc}$  distance) and the maximum absolute value of the asymmetry parameter was 0.68, which is much smaller than our maximum value. Figure 1 shows the histogram of the asymmetry parameter  $\delta V$  for the starless cores. The distribution is more skewed to negative values, suggesting that inward motions are more dominant than outward motions. [Lee et al. \(1999\)](#) studied low-mass starless cores at a spatial resolution of  $27''$  ( $0.020 \text{ pc}$  at  $150 \text{ pc}$  distance), and obtained a similar result. The range of the asymmetry parameter by them ranges from about  $-1.3$  to  $0.7$ , which is much narrower than our range. [Velusamy et al. \(2008\)](#) studied 27 cores in Orion in  $\text{HCO } J = 3 \rightarrow 2$  and reported inward motions in nine cores and outward motions in ten cores. at a spatial resolution of  $26''$  ( $0.053 \text{ pc}$  at  $420 \text{ pc}$  distance). Their  $\delta V$  ranges from  $-1.25$  to  $0.86$  with a bimodal distribution of blue and red. They regarded all the observed cores as starless, but in fact contains protostellar cores if we use the updated YSO information as noted before. There is only one core overlapping between our and their Orion cores. Their ORI1.9 and our core16 are the same protostellar core, and they consistently show red asymmetry suggesting expansion. [Jackson et al. \(2019\)](#) studied high-mass, dense molecular clumps and reported an overall blue asymmetry with a large sample of 1093 sources at a spatial resolution of  $38''$ .

First, we focused on cores whose  $v(\text{HCO}^+) - v(\text{H}^{13}\text{CO}^+)$  and  $v(\text{HCO}^+) - v(\text{N}_2\text{H}^+)$  are both  $\leq -0.2 \text{ km s}^{-1}$ . We assume that negative shifts more than twice the velocity resolution ( $0.1 \text{ km s}^{-1}$ ) are significant. Starless cores 5, 10, 11, 14, 17, 18, 20, 21, 23, 27, 28, and 32 (a total of 12 cores out of 30 or 40%) satisfy this condition.

Second, we investigate the  $\text{HCO}^+$ ,  $\text{H}^{13}\text{CO}^+$ , and  $\text{N}_2\text{H}^+$  profiles. To improve the signal-to-noise ratio, we collected data within a radius of  $10''$  (shown as the size of the plus sign, slightly larger than the telescope beam radius) on the Bessel-Gauss stacked pixel data. If the absorption is not strong enough, absorption may cause line asymmetry without a dip in the profile. The blue-skewed line profile with a dip is stronger evidence of possible inward motions than simple line profile asymmetry. Figures 2 to 4 shows the  $\text{HCO}^+$ ,  $\text{H}^{13}\text{CO}^+$ , and  $\text{N}_2\text{H}^+$  profiles toward cores which possibly show either blue-peaked or red-peaked  $\text{HCO}^+$  profiles. Again, we selected the isolated hyperfine component ( $F_1, F = 0, 1 \rightarrow 1, 2$ ), because we can avoid hyperfine component overlapping. The spectra may represent inward or outward motions, respectively. Among the 12 starless cores mentioned in the previous paragraph, we see hints of the blue-skewed line profile in cores 10, 11, 14, 17, 18, 21, and 32.

Third, we investigate stamp maps showing the spatial distribution of the  $\text{HCO}^+$  profiles on a grid of the sky coordinates. Figures 5 and 6 show  $5 \times 5$  stamp maps of  $\text{HCO}^+$  profiles on a grid of  $18''$  (approximately equal to the telescope beam size) centered at the core center position, for cores including the seven cores mentioned in the previous paragraph. The spectra are taken from the Bessel-Gauss stacked pixel data. The sky coordinates are shown as the intersection point of the profile coordinate axes. Cores 20 and 21 observed in the same field show two velocity components. Core 21 was judged to have two velocity components rather than a blue-skewed line profile with a dip.  $\text{N}_2\text{H}^+$  spectrum shown in Figure 3 support this interpretation. Now, we have six cores (cores 10, 11, 14, 17, 18, and 32) out of 30 (or 20%) as the  $\text{HCO}^+$  blue-skewed candidates. All the six cores show dips in the  $\text{HCO}^+$  spectra. However, for cores 17, 18, and 32, the S/N ratios in the  $\text{HCO}^+$  spectra are not high enough, or the sense of the line asymmetry is not observed consistently around the core center. Finally, we identify cores 10, 11, and 14 to have the  $\text{HCO}^+$  blue-skewed line profiles, while cores 17, 18, and 32 as “possibly blue-skewed line profiles.” Whenever the  $\text{HCO}^+$  profile represents blue-skewed or possibly blue-skewed line profiles with dips, we interpolated the profile from the outer part (open green circles in Figures 2 to 4). Here, we fixed the  $\text{HCO}^+$  Gaussian peak velocity to the value obtained from Gaussian fitting to the optically thinner,  $\text{H}^{13}\text{CO}^+$  emission. We determine the velocity range of absorption by comparing the  $\text{HCO}^+$  and  $\text{H}^{13}\text{CO}^+$  profiles. In other cases, we show the vertical lines of the  $\text{H}^{13}\text{CO}^+$  peak velocity (velocity corresponding to the intensity maximum), to illustrate the velocity difference of  $v(\text{HCO}^+) - v(\text{H}^{13}\text{CO}^+)$ . Core 12 in Figure 3 has two vertical lines, because the  $\text{H}^{13}\text{CO}^+$  profile has two maxima. All of our cores showing blue-skewed and possibly blue-skewed profiles satisfy the significance criterion for the asymmetry parameter of  $\delta V < -0.25$ . Out of the 30 observed cores, three cores (10%) are identified as cores having  $\text{HCO}^+$  (solid) “blue-skewed” profiles, and another three cores (10%) are identified as “candidate blue-skewed.” For the six cores of blue-skewed and possibly blue-skewed, the mean of the asymmetry parameter  $\delta V$  is  $-1.4 \pm 0.6$ . The core masses of these six blue-skewed cores including possible identification have a mean of  $1.94 M_{\text{odot}}$ , a median of  $1.45 M_{\text{odot}}$ , a minimum of  $0.15 M_{\text{odot}}$ , and a maximum of  $5.37 M_{\text{odot}}$  while the all the 30 starless cores have a mean of  $1.81 M_{\text{odot}}$ , a median of  $1.18 M_{\text{odot}}$ , a minimum of  $0.15 M_{\text{odot}}$ , and a maximum of  $7.1 M_{\text{odot}}$ . There is no preferred tendency in mass for the blue-skewed cores. Out of the six protostellar cores, four have negative  $\delta V$ , one (core 35) has  $\delta V = 0$ , and the remaining one (core 16) has a positive  $\delta V$ . Although the sample number of the protostellar core is small, we observe more cases with inward motions. None of the protostellar cores with blue-skewed profile, have dips in the spectra. Core 26 seems to have strong redshifted absorption, but also shows a prominent redshifted wing emission, which likely represents a molecular outflow.

Lastly, we investigated the core properties which are thought to be related to core evolutionary stages: the association with the core in  $\text{H}^{13}\text{CO}^+$  emission, detection in the dust continuum with the ALMA ACA, and the Chemical Evolution Factor, CEF2.0, based on the deuterium fraction. Association of the core in  $\text{H}^{13}\text{CO}^+$  emission is judged if there is a clear  $\text{H}^{13}\text{CO}^+$  emission peak within  $30''$  from the SCUBA-2 position. It is noted that we often observe offsets between the  $\text{H}^{13}\text{CO}^+$  emission peak and SCUBA-2 position. It is possible that depletion (Aikawa et al. 2001; Bergin & Tafalla 2002) of  $\text{H}^{13}\text{CO}^+$  affects its distribution. CEF2.0 and association of the core in  $\text{H}^{13}\text{CO}^+$  emission are listed in Table 7. Figures 7 to 12 show the velocity-integrated intensity map of the  $\text{H}^{13}\text{CO}^+$  emission toward the cores with either blue-peaked or red-peaked  $\text{HCO}^+$  profiles. Association with the core in  $\text{H}^{13}\text{CO}^+$  emission is listed in Table 7. ‘1’ means that the SCUBA-2 core is associated with the core in  $\text{H}^{13}\text{CO}^+$  emission, and ‘0’ means that it is not. All of the six cores of the blue-skewed or candidate blue-skewed line profiles with dips accompany  $\text{H}^{13}\text{CO}^+$  cores. It is known that the deuterium fractions of molecules formed in the gas phase (e.g.,  $\text{DNC}/\text{HNC}$  and  $\text{N}_2\text{D}^+/\text{N}_2\text{H}^+$ ) increase monotonically with core evolution during the starless core phase (Crapsi et al. 2005; Hirota & Yamamoto 2006; Emprechtinger et al. 2009; Feng et al. 2019). CEF2.0 is a measure of the chemical core evolution based on the logarithmic abundance ratio of  $\text{DNC}/\text{HNC}$  and  $\text{N}_2\text{D}^+/\text{N}_2\text{H}^+$ . The values of CEF2.0 were taken from Kim et al. (2020)



and [Tatematsu et al. \(2021\)](#). All the six cores have CEF2.0 values and they range from  $-58$  to  $-19$ . The association with the core in  $\text{H}^{13}\text{CO}^+$  emission and detection with ALMA ACA continuum may suggest that the six cores are at relatively late stages of the starless phase, but CEF2.0 values does not constrain that they are predominantly at extremely late stages. [Tokuda et al. \(2020\)](#) concluded that cores detected in the dust continuum with the ALMA ACA are at later stages during the starless core phase. [Sahu et al. \(2021\)](#) identified high-density structures, which are presumably at the latest stages of starless cores, with the ALMA in combination of the data of the 12 m Array C43-2 (TM2) configuration and the ACA. Table 3 lists ALMA core names used by them as well as those obtained from the ALMA Science Portal<sup>2</sup> for the sources which have been observed with the ALMA but have not been published yet.

The detection in the ALMA in the combined image from configuration TM2 and the ACA are reported by them, and listed as ‘TM2+ACA Detection.’ Regarding the ACA detectability ([Tokuda et al. 2020](#)), only one (core 14) out of the six was observed with ALMA ACA by [Dutta et al. \(2020\)](#), and this core was detected in the dust continuum, although the distance and sensitivity differ between these studies. Core 14 was not detected in TM2+ACA by [Sahu et al. \(2021\)](#).

<sup>2</sup> [almascience.org](https://almascience.org)

**Table 4.** Peak Intensity and Velocity

Core Number	HCO <sup>+</sup>		H <sup>13</sup> CO <sup>+</sup>		HNC		HN <sup>13</sup> C		N <sub>2</sub> H <sup>+</sup>	
	$T_A^*$	$v_{LSR}$	$T_A^*$	$v_{LSR}$	$T_A^*$	$v_{LSR}$	$T_A^*$	$v_{LSR}$	$T_A^*$	$v_{LSR}$
	K	km s <sup>-1</sup>	K	km s <sup>-1</sup>	K	km s <sup>-1</sup>	K	km s <sup>-1</sup>	K	km s <sup>-1</sup>
1	1.2	9.8	< 0.34	. . .	0.6	10.8	< 0.32	. . .	. . .	. . .
2	2.3	11.0	0.9	11.1	1.2	11.1	< 0.27	. . .	< 0.23	. . .
3	1.4	10.9	0.5	10.8	0.9	10.9	< 0.31	. . .	< 0.28	. . .
4	0.5	9.7	0.7	9.4	1.2	10.0	0.5	9.4	0.3	9.4
5	0.6	9.7	0.8	10.0	1.2	9.8	0.6	10.2	0.4	10.2
6	< 0.33	. . .	0.5	9.9	1.2	9.7	0.4	10.5	0.3	10.4
7	< 0.40	. . .	< 0.40	. . .	< 0.39	. . .	< 0.34	. . .	< 0.23	. . .
8	3.5	9.9	1.0	9.8	2.7	9.7	< 0.30	. . .	1.1	9.8
9	0.8	9.6	< 0.27	. . .	0.4	9.2	< 0.28	. . .	< 0.27	. . .
10	5.0	9.5	2.1	9.9	3.5	9.7	< 0.30	. . .	0.7	10.0
11	1.6	9.3	1.1	10.2	0.9	9.6	< 0.27	. . .	0.5	10.1
12	2.4	9.3	0.7	9.4	1.4	9.9	0.4	9.7	0.4	9.0
13	3.4	10.7	1.0	11.1	1.6	10.9	< 0.25	. . .	0.3	10.9
14	1.9	10.9	0.6	11.1	1.0	10.9	< 0.23	. . .	0.3	11.0
15	2.0	11.4	0.5	11.2	1.3	11.4	< 0.27	. . .	0.4	11.3
16	4.7	11.4	3.2	11.1	3.7	11.4	0.9	11.1	3.9	11.2
17	0.8	7.7	0.7	8.2	1.0	8.4	< 0.25	. . .	0.3	8.2
18	1.0	7.6	0.7	7.8	0.9	7.6	< 0.22	. . .	0.4	7.8
19	1.9	8.4	0.5	8.6	1.3	8.5	0.4	8.8	0.7	8.5
20	2.5	7.4	1.0	7.6	1.0	7.0	< 0.29	. . .	0.4	7.9
21	2.2	7.6	1.1	8.1	1.6	7.5	< 0.25	. . .	0.5	8.9
22	1.6	8.0	0.8	8.2	1.1	8.0	< 0.44	. . .	0.5	8.2
23	0.8	7.9	0.3	8.3	1.1	8.9	< 0.27	. . .	0.6	8.3
24	1.2	8.3	0.6	8.1	1.3	8.6	0.5	7.9	0.9	8.0
25	1.4	7.8	0.6	7.6	1.6	7.6	0.4	8.3	0.5	7.7
26	2.6	7.8	1.0	8.2	2.7	7.8	0.6	8.0	0.6	8.1
27	3.3	5.5	1.1	5.9	2.4	5.5	0.4	5.7	0.4	5.8
28	1.5	7.4	1.2	8.1	2.3	7.3	0.7	8.1	0.5	8.2
29	1.8	6.4	0.4	6.4	1.3	6.4	< 0.37	. . .	0.2	6.3
30	1.8	5.6	1.1	5.1	1.9	5.4	0.4	5.4	0.5	5.2
31	1.7	4.0	0.9	4.3	2.1	4.0	0.4	4.5	0.9	4.3
32	1.7	3.0	0.7	3.3	1.6	3.1	0.4	3.4	0.7	3.3
33	1.7	4.2	0.7	4.4	1.5	4.2	< 0.30	4.3	0.4	4.5
34	< 0.39	. . .	< 0.39	. . .	< 0.39	. . .	< 0.50	. . .	< 0.18	. . .
35	1.5	3.9	0.9	3.9	2.5	4.0	0.7	4.0	0.5	4.2
36	1.1	11.2	< 0.47	. . .	1.2	11.2	< 0.55	. . .	0.5	11.5

**Table 5.** Number of Velocity Components

Core Number	H <sup>13</sup> CO <sup>+</sup>	N <sub>2</sub> H <sup>+</sup>
1	. . .	. . .
2	1	. . .
3	1	. . .
4	1	1
5	1	1
6	2	1
7	. . .	. . .
8	1	1
9	. . .	. . .
10	1	1 or 2
11	1	1
12	2	1
13	1	1 or 2
14	1 or 2	1
15	1 or 2	1
16	1	1
17	1	1
18	1	1
19	1	1
20	1	1
21	complicated	1-3
22	1	1
23	1	1
24	1	1
25	2	2
26	1	1
27	1	1
28	3	2
29	1	. . .
30	1	1
31	1	1
32	1	1
33	1	1
34	. . .	1
35	1	1
36	1	1

**Table 6.** Velocity Difference and Core Properties

Core Number	YSO Ass.	$v(\text{HCO}^+) - v(\text{H}^{13}\text{CO}^+)$ km s <sup>-1</sup>	$v(\text{HCO}^+) - v(\text{N}_2\text{H}^+)$ km s <sup>-1</sup>	$v(\text{HNC}) - v(\text{HN}^{13}\text{C})$ km s <sup>-1</sup>	$\Delta v(\text{H}^{13}\text{CO}^+)$ km s <sup>-1</sup>	$\delta V$
1	starless	...	...	...	...	...
2	starless	-0.1	...	...	0.19	-0.5
3	starless	0.1	...	...	0.33	0.3
4	starless	0.3	0.3	0.6	0.21	1.4
5	starless	-0.3	-0.5	-0.4	0.54	-0.6
6	starless	...	...	-0.8	0.46	0.0
7	starless	...	...	0.0	...	...
8	starless	0.1	0.1	...	0.25	0.4
9	starless	...	...	...	...	...
10	starless	-0.4	-0.5	...	0.39	-1.0
11	starless	-0.9	-0.8	...	0.38	-2.4
12	starless	-0.1	0.3	0.2	0.61	(-0.2)
13	protostellar	-0.4	-0.2	...	0.30	-1.3
14	starless	-0.2	-0.1	...	0.34	(-0.6)
15	starless	0.2	0.1	...	0.38	(0.5)
16	protostellar	0.3	0.2	0.3	0.32	0.9
17	starless	-0.5	-0.5	...	0.24	-2.1
18	starless	-0.2	-0.2	...	0.18	-1.1
19	starless	-0.2	-0.10	-0.3	0.27	-0.8
20	starless	-0.2	-0.5	...	0.72	-0.3
21	starless	-0.5	-1.3	...	0.65	(-0.8)
22	starless	-0.2	-0.2	...	0.14	-1.4
23	starless	-0.4	-0.4	...	0.12	-3.2
24	starless	0.2	0.3	0.7	0.24	0.8
25	starless	0.2	0.1	-0.7	0.35	(0.6)
26	protostellar	-0.4	-0.3	-0.2	0.31	-1.3
27	starless	-0.4	-0.3	-0.2	0.36	-1.1
28	starless	-0.7	-0.8	-0.8	0.46	(-1.5)
29	starless	0.0	0.1	...	0.16	0.0
30	starless	0.5	0.4	0.0	0.21	2.3
31	protostellar	-0.3	-0.3	-0.5	0.34	-0.9 ...
32	starless	-0.3	-0.3	-0.3	0.23	-1.3
33	protostellar	-0.2	-0.3	-0.1	0.31	-0.6
34	starless	...	...	...	...	...
35	protostellar	0.0	-0.3	0.0	0.32	0.0
36	starless	...	-0.3	...	0.29	...

**Table 7.** Velocity Difference and Core Properties

Core Number	Core in H <sup>13</sup> CO <sup>+</sup> Emission	SCUBA-2 Filament	ACA Detection	TM2+ACA Detection	CEF2.0
1	...	0	NO (weak?)	NO	...
2	1	0	NO	NO	...
3	1	0	NO (weak?)	NO	...
4	1	0	...	...	-43 ± 27
5	1	1	NO (weak?)	NO	...
6	0	1	YES	NO	...
7	0	1	YES	YES	...
8	1	1	YES	NO	...
9	0	1	YES	NO	...
10	1	0	...	...	-41 ± 27
11	1	1	...	...	-27 ± 14
12	1	1	NO	NO	-34 ± 3
13	1	1	YES	NO	...
14	1	1	YES	NO	...
15	1	0	NO	NO	-41 ± 8
16	1	1	YES	YES	...
17	1	1	...	...	-19 ± 15
18	1	1	...	...	-20 ± 19
19	0	1	YES (weak?)	NO	-58 ± 17
20	1	1	YES	YES	-42 ± 5
21	1	1	NO (weak?)	NO	...
22	0	1	YES	NO	-27 ± 15
23	0	0	...	...	-56 ± 27
24	0	1	NO	NO	-50 ± 27
25	0	1	YES	NO	...
26	1	1	YES	YES	...
27	1	0	NO (weak?)	NO	-37 ± 14
28	1	1	YES (weak?)	NO	-22 ± 20
29	0	0	YES	NO	-7 ± 28
30	0	1	YES	NO	-24 ± 14
31	1	1	YES	NO	...
32	1	1	...	...	-22 ± 5
33	1	1	YES (weak)	NO	...
34	...	1	...	...	...
35	1	1	YES	YES	...
36	0	0	YES (weak?)	NO	...



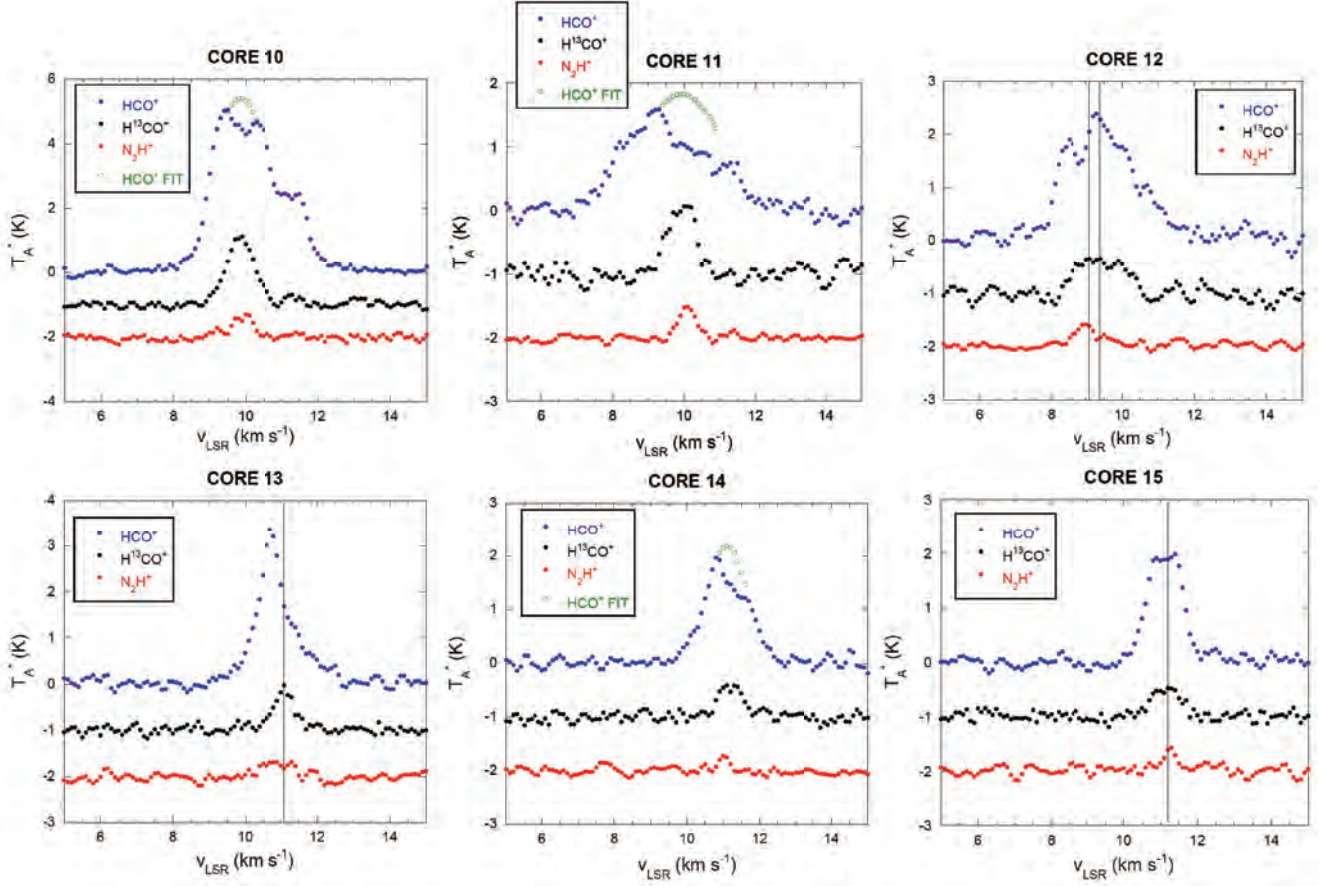


**Figure 2.**  $\text{HCO}^+$  (filled blue circles),  $\text{H}^{13}\text{CO}^+$  (filled black circles), and  $\text{N}_2\text{H}^+$  (filled red circles) profiles toward cores 10, 11, 12, 13, 14 and 15. The open green circles show interpolated Gaussian fitting to the  $\text{HCO}^+$  profile by fixing the line center velocity to the Gaussian fitted peak velocity of the  $\text{H}^{13}\text{CO}^+$  emission for the blue-skewed profile cores. The vertical line shows the peak velocity of the  $\text{H}^{13}\text{CO}^+$  emission for the other cores.

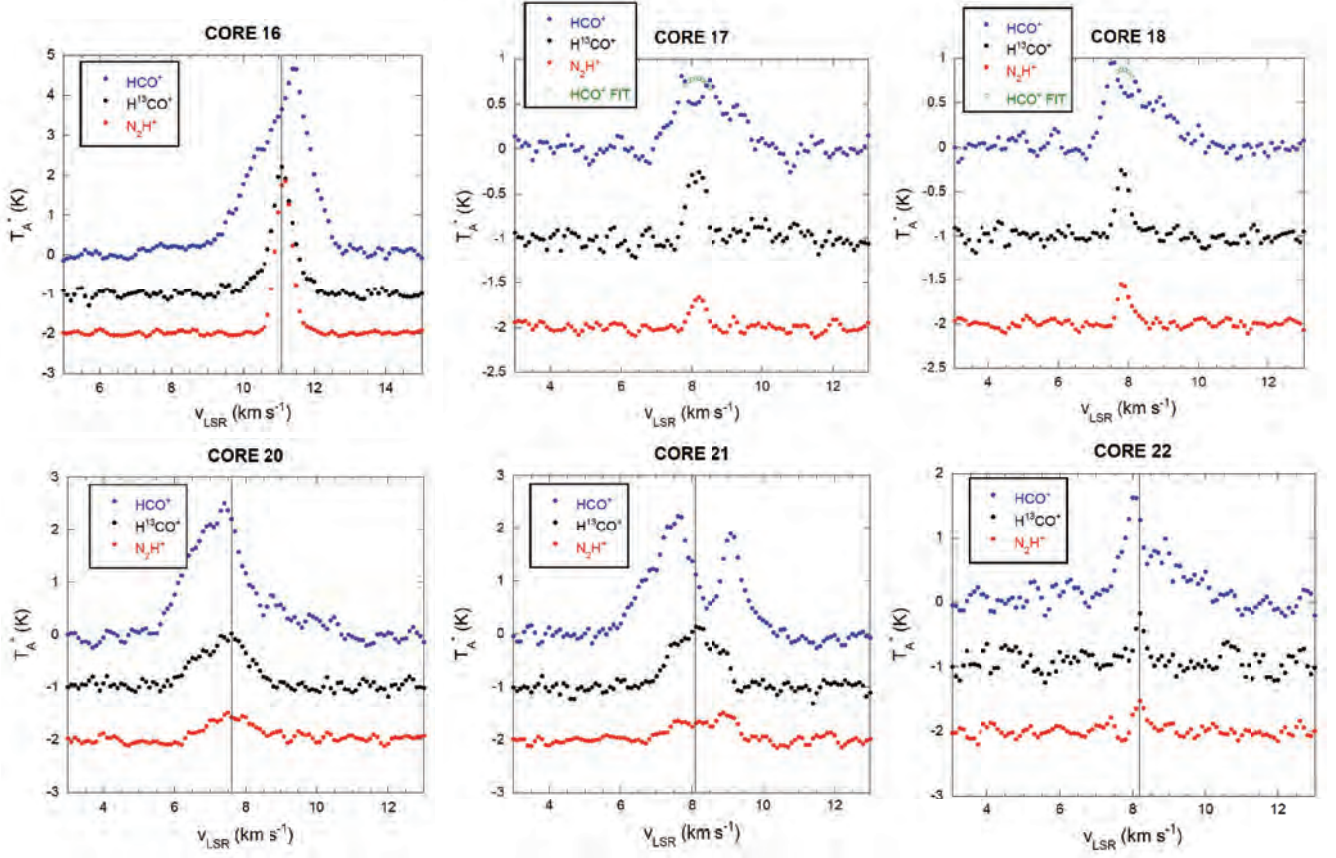


**Figure 3.** The same as Figure 2 but for cores 16, 17, 18, 20, 21, and 22. For clarity, the lines connecting the plots are added for core 16.

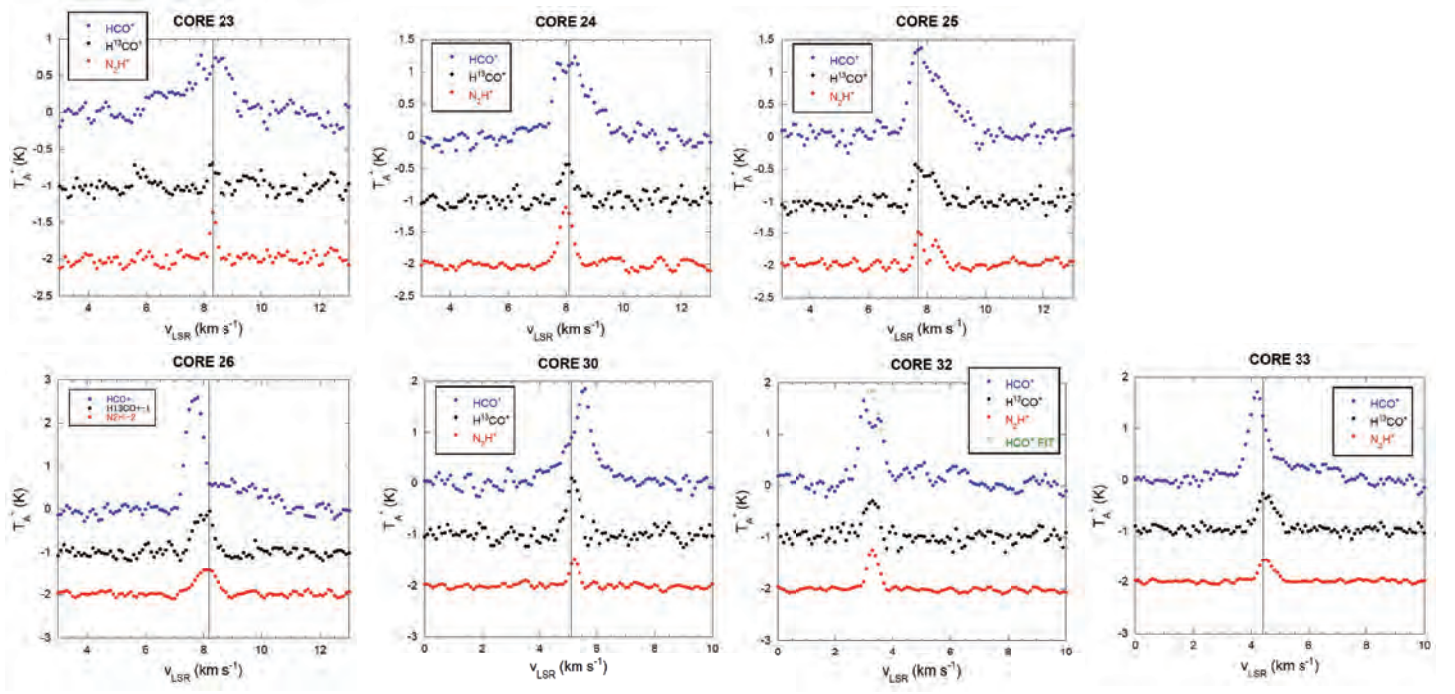


**Figure 4.** The same as Figure 2 but for cores 23, 24, 25, 26, 30, 32, and 33.

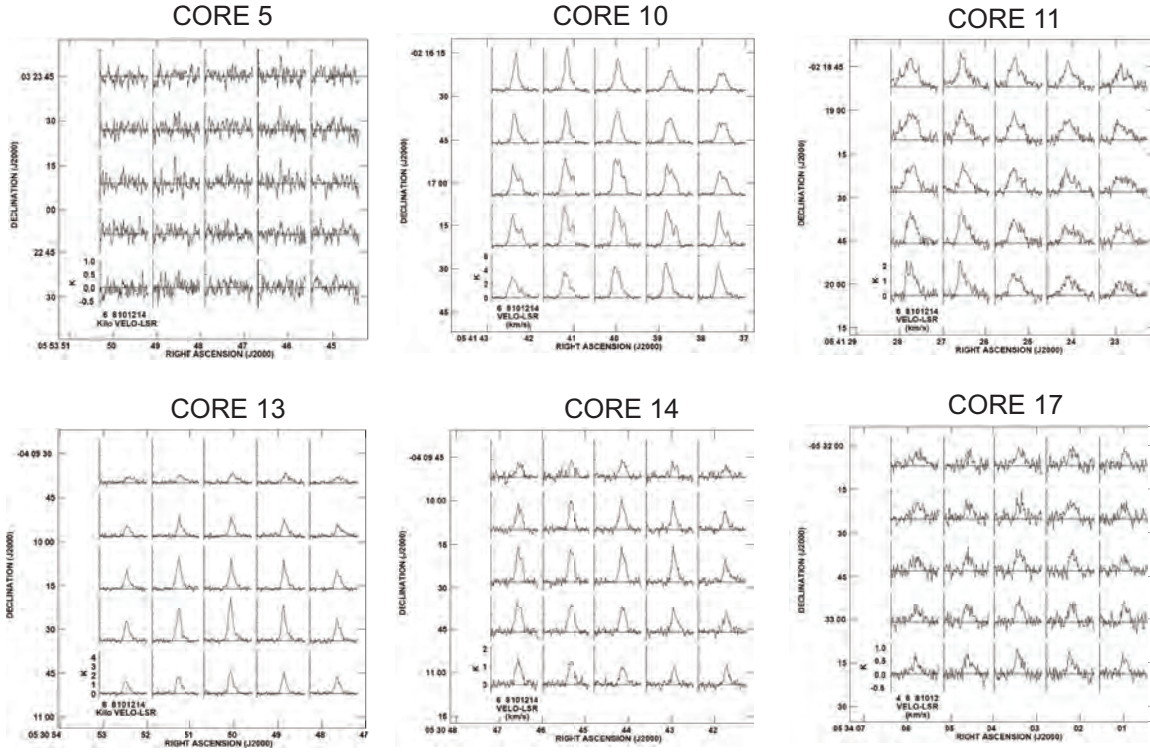


**Figure 5.** The stamp map of the HCO<sup>+</sup> emission toward cores 5, 10, 11, 13, 14, and 17.



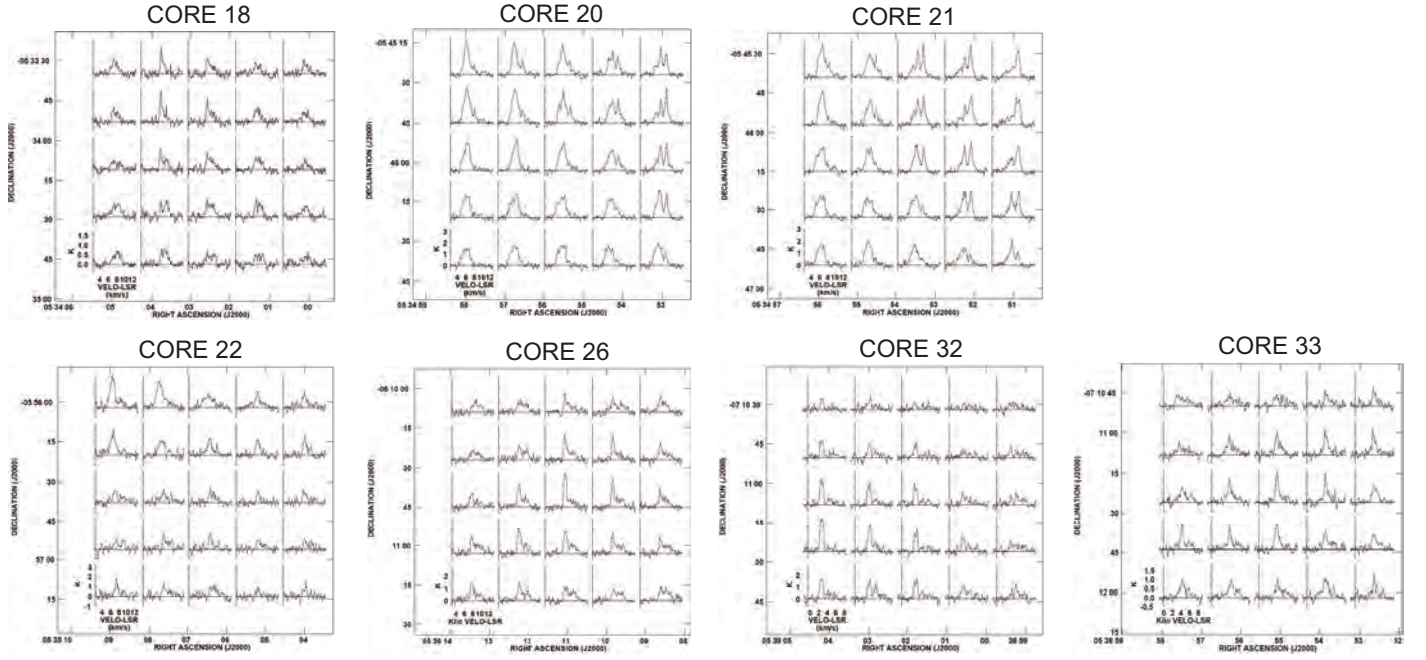


**Figure 6.** The same as Figure 5 but for cores 18, 20, 21, 22, 26, 32, and 33.



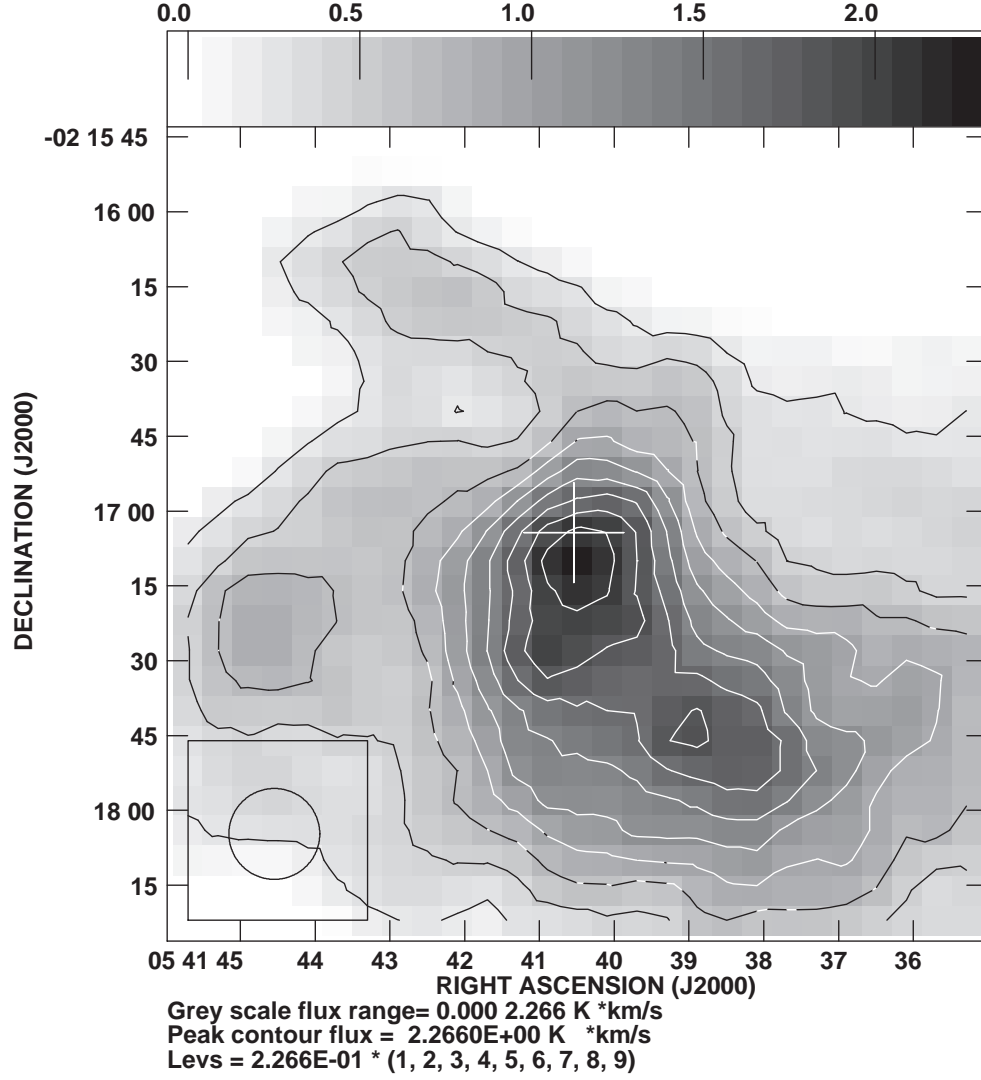


**Figure 7.** Gray-scale map of the velocity integrated intensity of the  $\text{H}^{13}\text{CO}^+$  emission toward core 10 (G206.93–16.61East1). The plus sign represents the SCUBA-2 core center position, and its maximum size ( $20''$ ) represents the diameter of the circular area we collected data for a composite spectrum such as Figure 2. The circle in the bottom-left corner represents the half-power beam size ( $18''.2$  diameter).

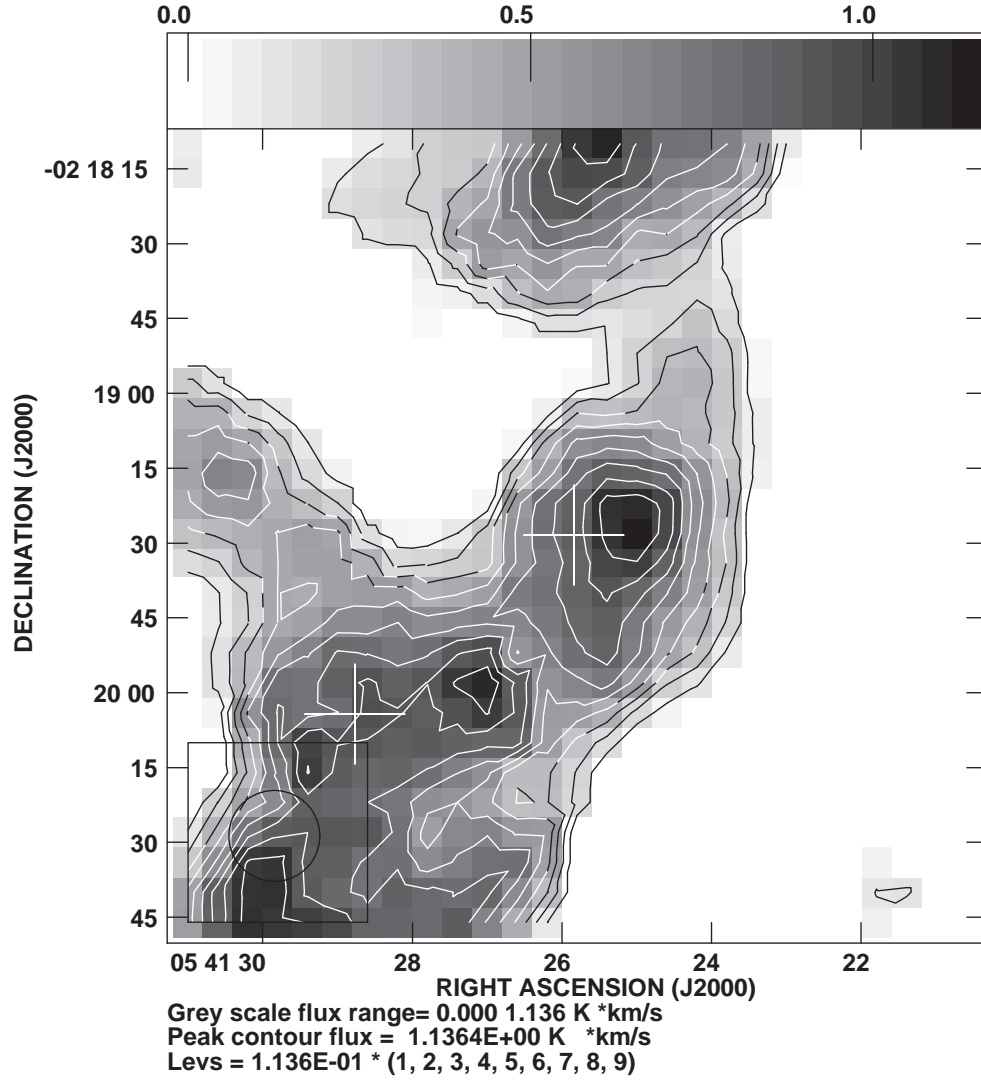


**Figure 8.** The same as Figure 7 but for core 11 (G206.93–16.61West4) at the center and core 12 (G206.93–16.61West5) on its south-eastern side.

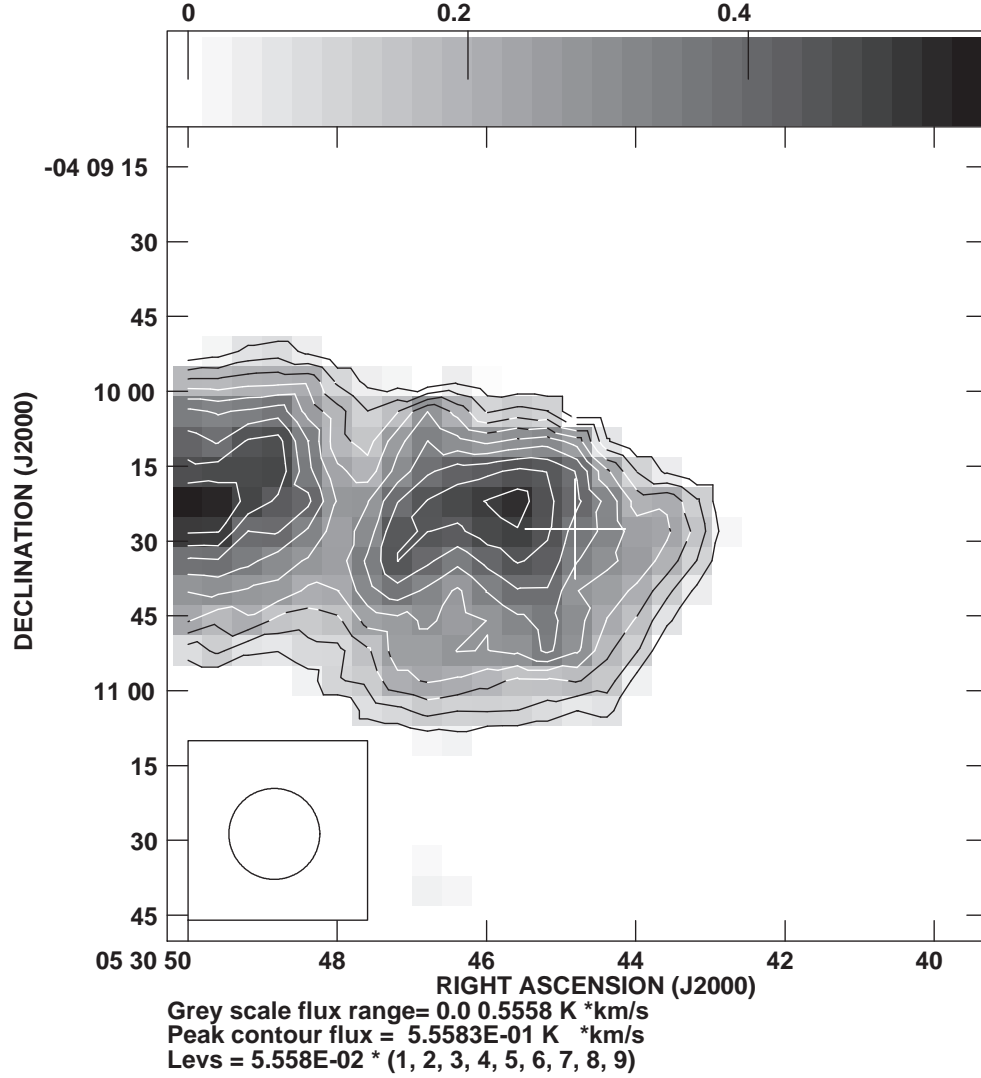


**Figure 9.** The same as Figure 7 but for core 14 (G207.36–19.82North4).

(a) Core 10 (G206.93–16.61East1)

This core belongs to NGC 2023 in the Orion B cloud. Figure 5 shows complicated profiles. It seems that this region contains another velocity component at  $\sim 11.5 \text{ km s}^{-1}$ . However, we observe double-peaked profile separately and clearly, and the peak velocity of the  $\text{H}^{13}\text{CO}^+$  emission well corresponds to that of the dip. Table 5 lists one or two

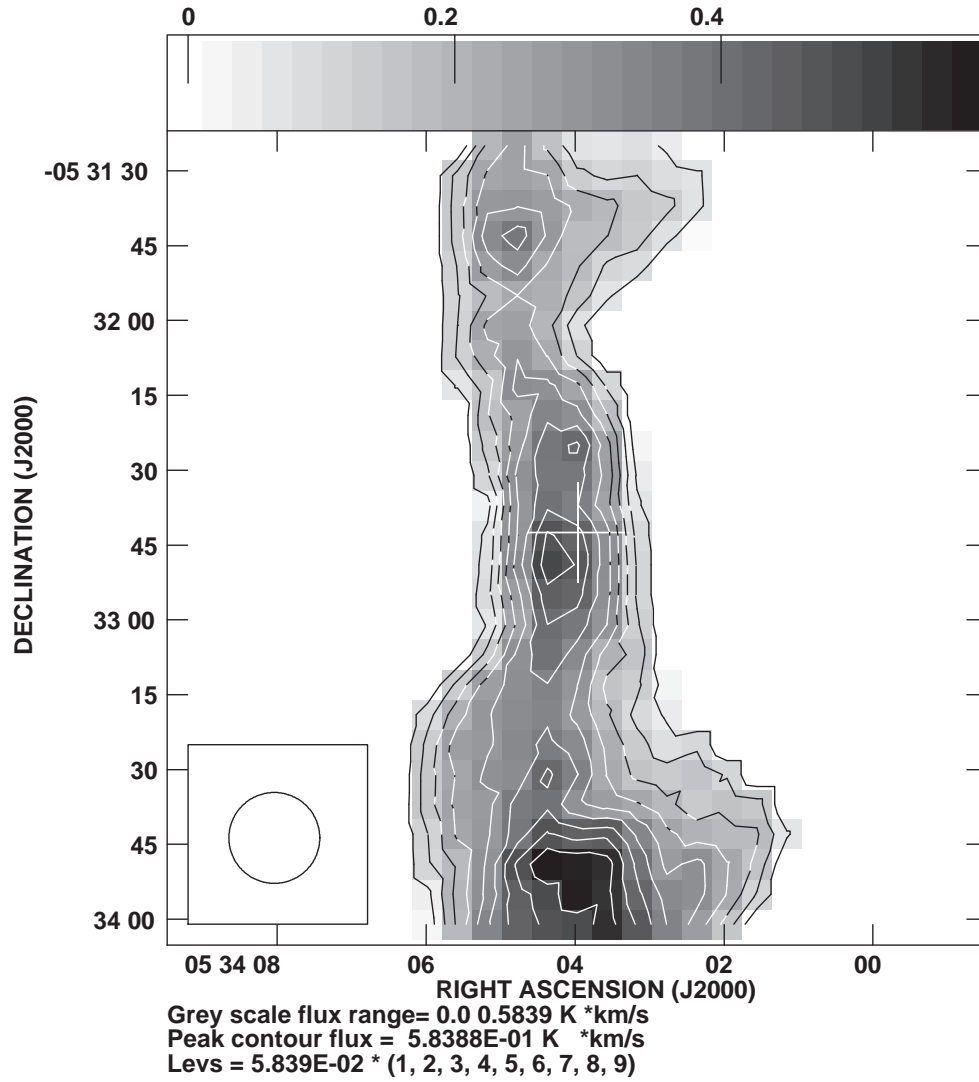


**Figure 10.** The same as Figure 7 but for core 17 (G209.05–19.73North).

velocity components in  $\text{H}^{13}\text{CO}^+$ , but the velocity difference between the two velocity components is very small. This will not affect our interpretation.

(b) Core 11 (G206.93–16.61West4)

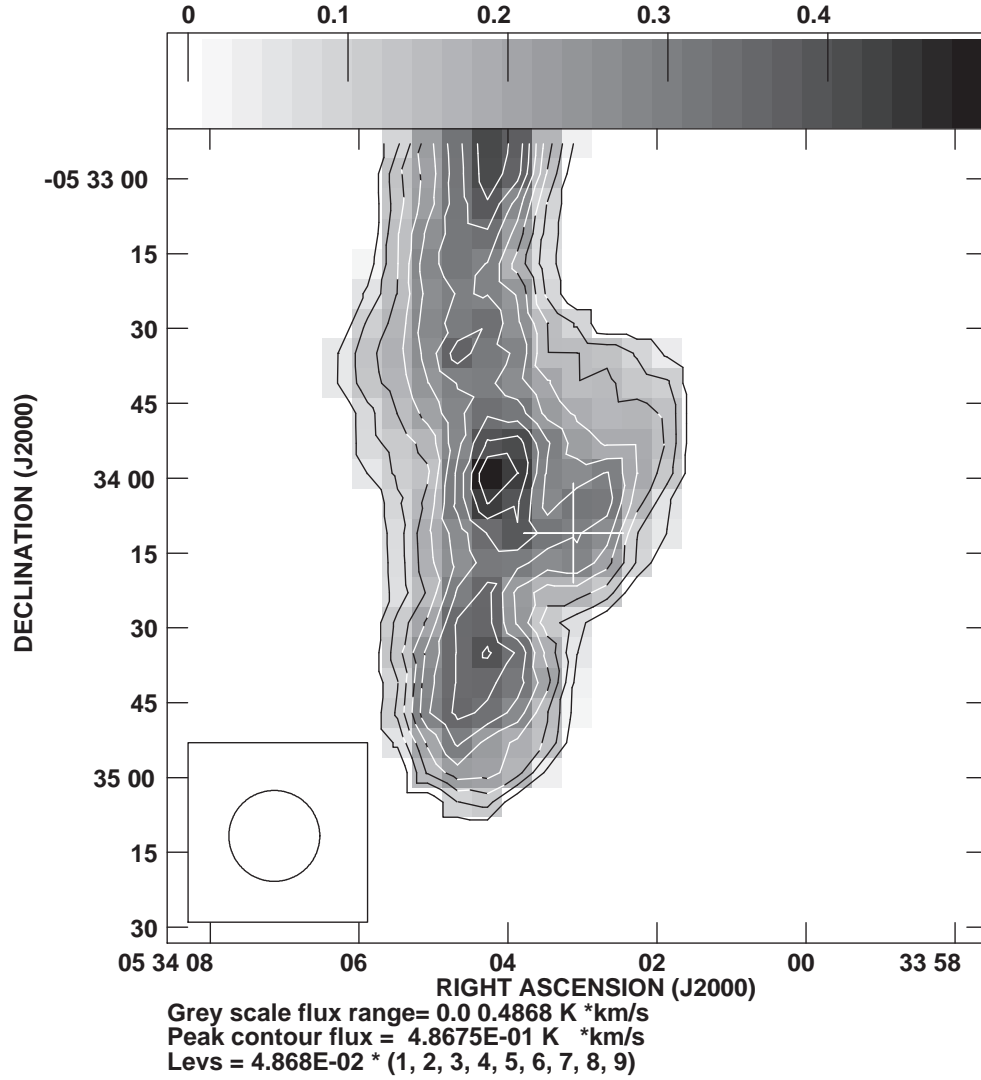


**Figure 11.** The same as Figure 7 but for core 18 (G209.05–19.73South).

290 This core belongs to NGC 2023 in the Orion B cloud, and is close to core 10. This is a clear case of the blue-skewed  
291 line profile with a dip. Figure 5 shows that the S/N ratio of the observed spectrum is not very good. However, Figure  
292 2 shows that the peak velocities of the  $\text{H}^{13}\text{CO}^+$  and  $\text{N}_2\text{H}^+$  emissions are consistent. On the other hand, that of the  
293  $\text{HCO}^+$  emission is apparently blue-shifted.



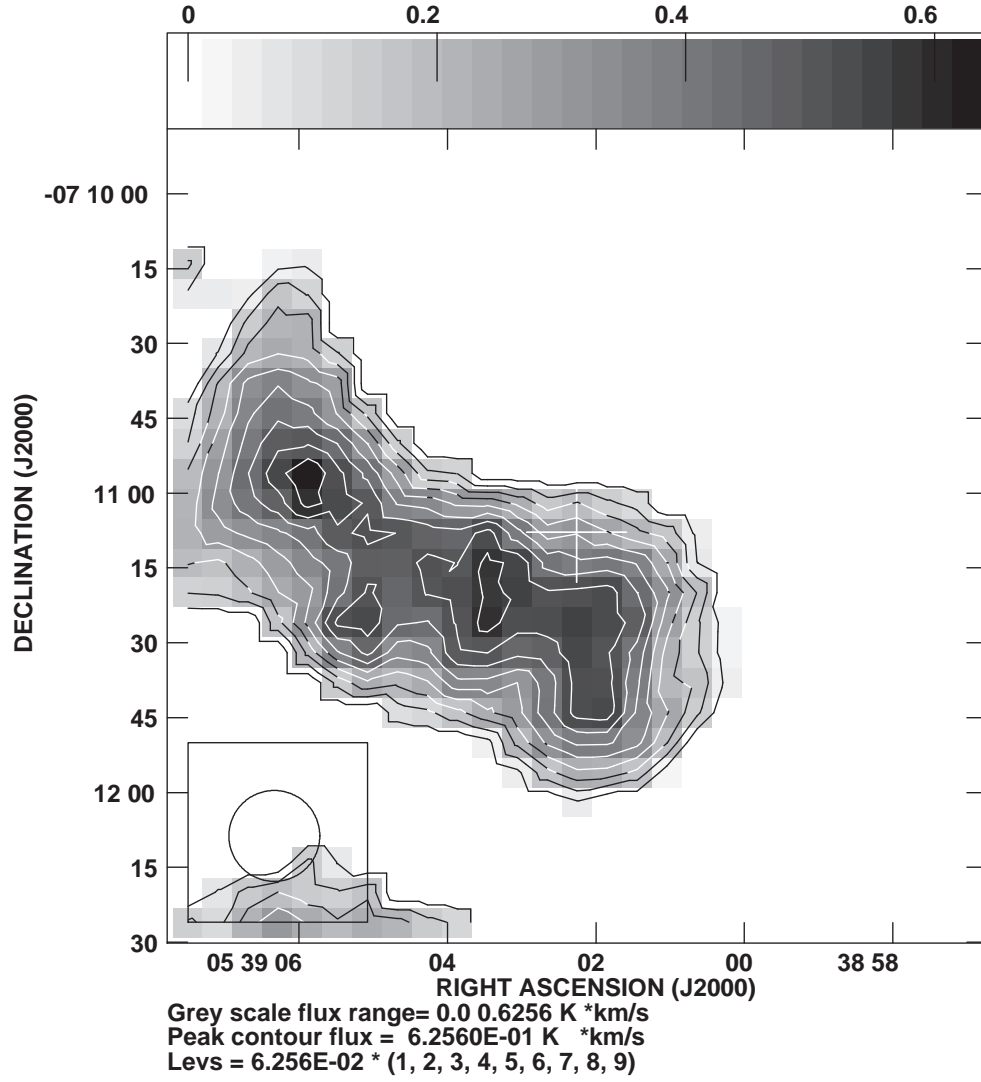


**Figure 12.** The same as Figure 7 but for core 32 (G211.16–19.33North3).

(c) Core 13 (G207.36–19.82North2)

This core is located in the northern end of the Orion A cloud. This is a clear case of the blue-skewed line profile without a dip.

(d) Core 14 (G207.36–19.82North4)

**Table 8.** HCO<sup>+</sup> Absorption Strength

Core Number	Dip Integ. Intensity K km s <sup>-1</sup>	Dip Width km s <sup>-1</sup>	HCO <sup>+</sup> Fit Intensity K
10	0.52	0.10	5.42
11	1.09	0.60	1.83
14	0.52	0.23	2.28
17	0.11	0.14	0.79
18	0.11	0.13	0.88
32	0.18	0.10	1.86

This core is located in the northern end of the Orion A cloud, and close to core 13. This is a clear case of the blue-skewed line profile with a dip. Figure 5 shows that we see doubly-peaked profile around the core center. We observe it also on the eastern side of the figure.

(e) Core 17 (G209.05–19.73North)

This core belongs to OMC-4 in the integral-shaped filament in the Orion A cloud. Figure 5 shows that the S/N ratio of the observed spectrum is not very good. Figure 3 shows that the blue peak of the doubly-peaked HCO<sup>+</sup> profile is only slightly brighter than the red peak. However, Figure 3 shows that the peak velocity of the H<sup>13</sup>CO<sup>+</sup> emission well corresponds to that of the dip. The peak velocities of the H<sup>13</sup>CO<sup>+</sup> and N<sub>2</sub>H<sup>+</sup> emission are consistent.

(f) Core 18 (G209.05–19.73South)

This core belongs to OMC-4 in the integral-shaped filament in the Orion A cloud, and close to core 17. Figure 5 shows that the S/N ratio of the observed spectrum is not very good. However, Figure 3 shows that the peak velocities of the H<sup>13</sup>CO<sup>+</sup> and N<sub>2</sub>H<sup>+</sup> emission are consistent. On the other hand, that of the HCO<sup>+</sup> emission is apparently blue-shifted.

(g) Core 26 (G209.94–19.52North)

This core belongs to L1641 in the Orion A cloud. This is a clear case of the blue-skewed line profile without a dip.

(h) Core 32 (G211.16–19.33North3)

This core belongs to L1641 in the Orion A cloud. Figure 6 shows that we observe doubly peaked profiles at the core center and on the eastern side of the figure. The sense of the asymmetry is blue-skewed toward the core center, but is opposite at neighboring positions. This core was previously observed with the ALMA ACA (Tatematsu et al. 2020), and the blue-skewed line profile with a dip was detected in DCO<sup>+</sup>  $J = 3 \rightarrow 2$ .

(i) Core 33 (G211.16–19.33North4)

This core belongs to L1641 in the Orion A cloud. This is a clear case of the blue-skewed line profile without a dip.

### 3.3. Some Notes on Specific Cores

Toward core 6 (G203.21–11.20East1), we did not detect the HCO<sup>+</sup> emission, although we detected the H<sup>13</sup>CO<sup>+</sup> emission. It seems that the HCO<sup>+</sup> intensity sharply drops toward the east around R.A. = 5<sup>h</sup>53<sup>m</sup>50<sup>s</sup>. We observe an absorption dip in HCO<sup>+</sup> around core 5 (Figure 5), suggesting contamination of the line emission at the reference off position. Li et al. (2021) observed a similar situation in their observation with the ALMA that the cold core M1 in NGC6334S shows strong H<sup>13</sup>CO<sup>+</sup> emission, but does not do HCO<sup>+</sup> emission.

Core 9 (G206.21–16.17South) does not show H<sup>13</sup>CO<sup>+</sup> emission. The intensity of the HCO<sup>+</sup> emission and N<sub>2</sub>H<sup>+</sup> is weak (0.8 K and 0.2 K, respectively). Instead, we observe a local peak  $\sim 40''$  east of the nominal SCUBA-2 position (see Figure 19.3 in Tatematsu et al. 2021). Dutta et al. (2020) detected the continuum emission with the ALMA ACA toward this eastern position as G206.21–16.17S.

Core 23 (G209.77–19.40West) has a large velocity difference between HCO<sup>+</sup> and H<sup>13</sup>CO<sup>+</sup>. It has two velocity peaks in HCO<sup>+</sup>. However, the profile does not show a blue-skewed profile. We do not identify a core in H<sup>13</sup>CO<sup>+</sup> emission here.

## 4. DISCUSSION

#### 4.1. $\text{HCO}^+$ Absorption Strength and Likely Periods of Infall Motions

We wonder whether inward motions occur at specific periods in the starless core phase or not. Regarding the core evolutionary stages, we use the core density and CEF2.0. Both of them are supposed to increase with evolution. We adopt the integrated intensity of the absorption dip in the  $\text{HCO}^+$  spectrum as the strength of absorption. We measure the integrated intensity enclosed between the  $\text{HCO}^+$  profile (filled blue circles) and the interpolated profiles (open green circles) in Figures 2, 3, and 4. We also calculate the dip width which is the dip integrated intensity divided by the  $\text{HCO}^+$  peak intensity estimated from interpolated Gaussian fitting. The dip width is a kind of the “equivalent width” expressed in velocity units. Table 8 lists the dip integrated intensity and dip width in the  $\text{HCO}^+$  emission.

Figures 13 and 14 plot the core radius and density from the SCUBA-2 observations against the  $\text{HCO}^+$  dip integrated intensity. Larger symbols present blue-skewed cores, while smaller symbols represent candidate blue-skewed cores. It seems that the core radius decreases and the core density increases with increasing  $\text{HCO}^+$  dip integrated intensity. If we assume the increase in the core density represents the core evolution, the  $\text{HCO}^+$  dip integrated intensity increases with core evolution, and the core radius decreases with core evolution. However, if we take only the blue-skewed cores, the above trend is not very clear. Figures 15 and 16 are the same as Figures 13 and 14 but for the dip width as an abscissa axis. The above trend is not very clear. We would conclude that we do not see strong evidence for evolutionary change in the  $\text{HCO}^+$  absorption strength.

Next, we investigate the speed of inward motions. Three-dimensional fields of density and velocity of inward motions and relation with the line of sight as well as radiative transfer will determine the actual line profile. For simplicity, we take the velocity difference,  $v(\text{HCO}^+) - v(\text{H}^{13}\text{CO}^+)$ , as a maximum velocity extent of inward motions. The absolute value of  $v(\text{HCO}^+) - v(\text{H}^{13}\text{CO}^+)$  of the six cores with the blue-skewed or candidate blue-skewed ranges from 0.2 to 0.9  $\text{km s}^{-1}$ .  $v(\text{HCO}^+)$  is for the intenser peaks of the double peaks. Again, the lower limit of 0.2  $\text{km s}^{-1}$  comes from the significance criterion, and we cannot detect subsonic motions well. The sound speed of the gas at a temperature of 10 K of a mean molecular weight per particle of 2.33  $m_{\text{H}}$  and corresponding FWHM velocity width are 0.19  $\text{km s}^{-1}$  and 0.44  $\text{km s}^{-1}$ , respectively. Then, the absolute value of the  $v(\text{HCO}^+) - v(\text{H}^{13}\text{CO}^+)$  suggests that inward motions may include supersonic values.

Figures 17 and 18 plot CEF2.0 against the dip integrated intensity and dip width, respectively. Note that CEF2.0 is defined as an increasing function of the time evolution so that CEF2.0 in starless cores ranges from  $\sim -100$  to  $\sim 0$ . We do not see a clear correlation. Given that CEF2.0 represents core evolution, the dip integrated intensity or dip width do not preferably appear at specific times during the evolution of the starless core phase. Therefore, we have no strong evidence that inward motion phenomena are observed predominantly at the latest stage in the starless phase.

For starless dark cloud cores, Shirley et al. (2005) suggested the evolutionary sequence from L1521B, then L1498, and to L1544 with chemical evolution signatures (Lee et al. 2003), with increasing density and also with increasing central condensation in the dust continuum emission distribution. Hirota & Yamamoto (2006) suggested a consistent evolutionary sequence for these objects, and the deuterium fraction increases in this order. CEF2.0 is defined as an increasing function of the deuterium fraction. However, Figure 19 does not show that density increases with CEF2.0 or the deuterium fraction. We wonder whether starless Orion cores evolve like starless dark cloud cores or not. Figures 20 and 21 show the relationship between CEF2.0, core density, the velocity difference between  $\text{HCO}^+$  and  $\text{H}^{13}\text{CO}^+$ , and the  $\text{H}^{13}\text{CO}^+$  line width. We cannot see outstanding trends except for the  $\text{H}^{13}\text{CO}^+$  line width against density; the  $\text{H}^{13}\text{CO}^+$  line width seems to increase with density. If starless core dissipate turbulence toward star formation, the line width may decrease with time. If density increases during starless core evolution, the Figure suggests that the line width also increases. We may need to investigate which is the best evolutionary tracer for the evolution of starless cores in Orion. The density range suggested by Shirley et al. (2005) is from  $< 10^4 \text{ cm}^{-3}$  to  $10^6 \text{ cm}^{-3}$ . On the other hand, the density range studied by Yi et al. (2018) is from  $10^5 \text{ cm}^{-3}$  to  $10^6 \text{ cm}^{-3}$ . Crapsi et al. (2005) compared the deuterium fraction on the basis of  $\text{N}_2\text{D}^+$  and chemical simulation, and it seems that derived values match simulations from  $10^2 \text{ cm}^{-3}$  to  $10^4 \text{ cm}^{-3}$ . Density may depends on not only core evolution stages but also local environments for cores. Then, it is not unlikely that a variation of the core density in a narrower range may have a limited reliability as an evolutionary stage tracer.

#### 4.2. Reliability of the blue-skewed line profile with a dip

Signatures of the blue-skewed or candidate blue-skewed line profiles with dips in the present study are not very convincing as they are. Independent observations of relevant molecules and in appropriate transitions are desirable. Chira et al. (2014) suggested to use optically thicker high-J transitions such as  $J = 3 \rightarrow 2$ ,  $J = 4 \rightarrow 3$ , and  $J = 5 \rightarrow 4$

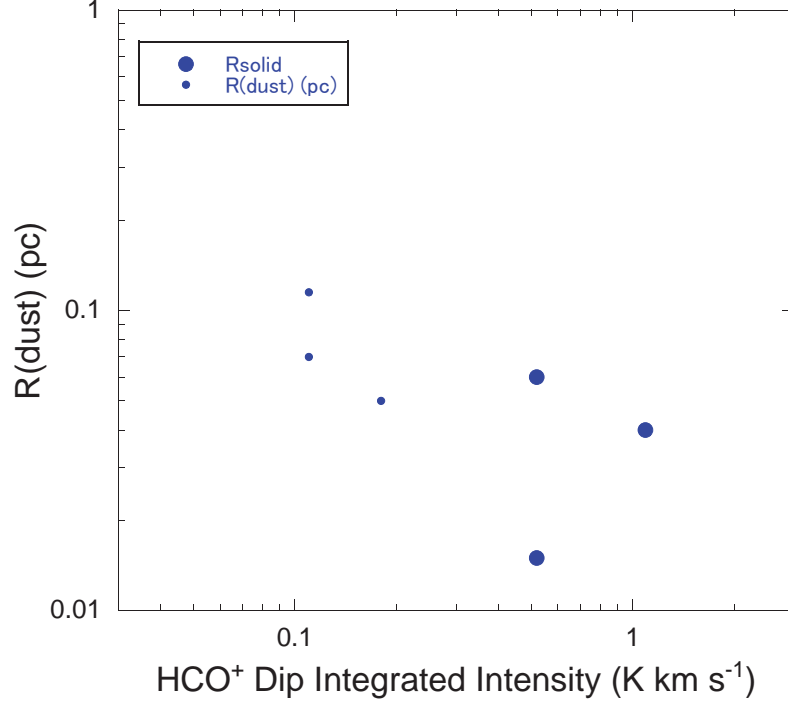


**Figure 13.** Core radius is plotted against the HCO<sup>+</sup> dip integrated intensity. The larger symbols represent the blue-skewed cores, while the smaller symbols the candidate blue-skewed cores.

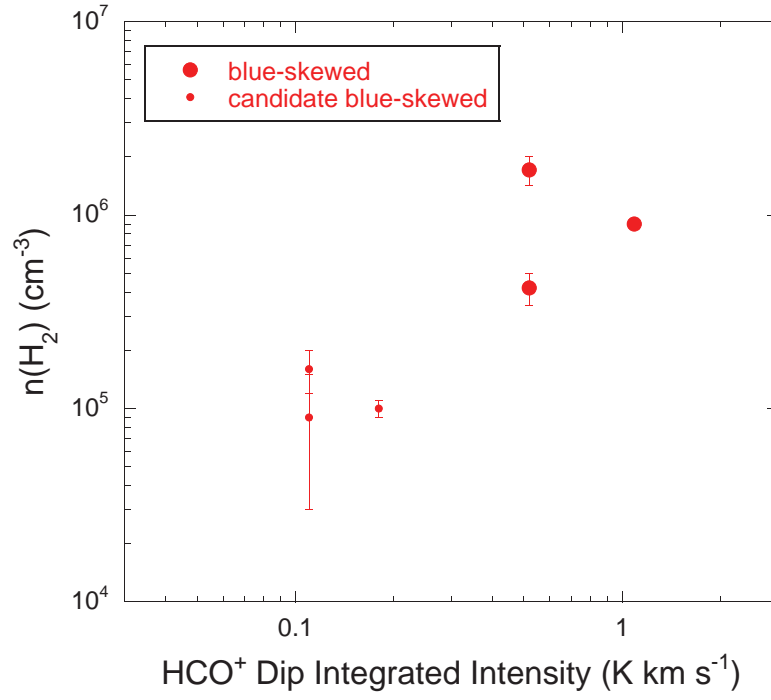


**Figure 14.** Core density is plotted against the HCO<sup>+</sup> dip integrated intensity. The larger symbols represent the blue-skewed cores, while the smaller symbols the candidate blue-skewed cores.

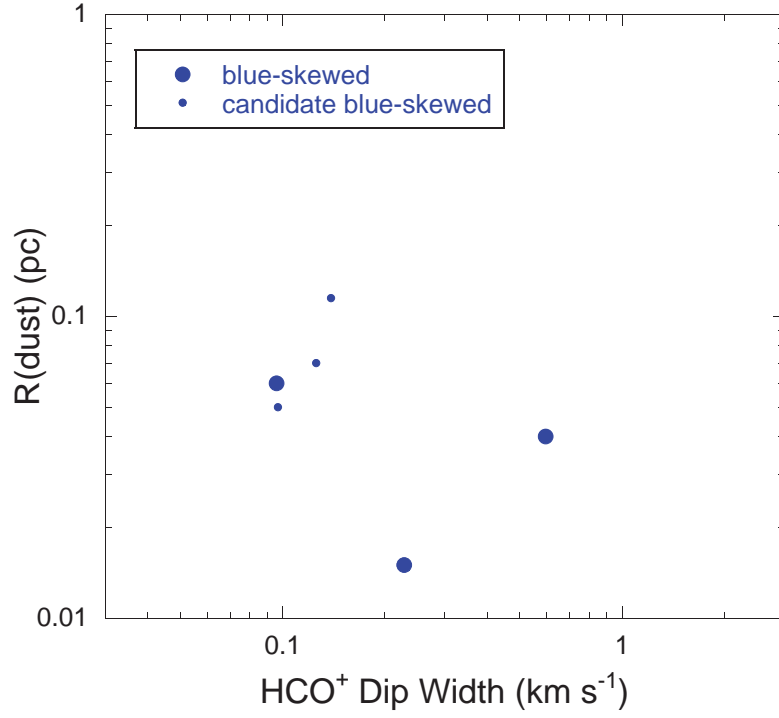


**Figure 15.** Core radius is plotted against the  $\text{HCO}^+$  dip width. The larger symbols represent the blue-skewed cores, while the smaller symbols the candidate blue-skewed cores.

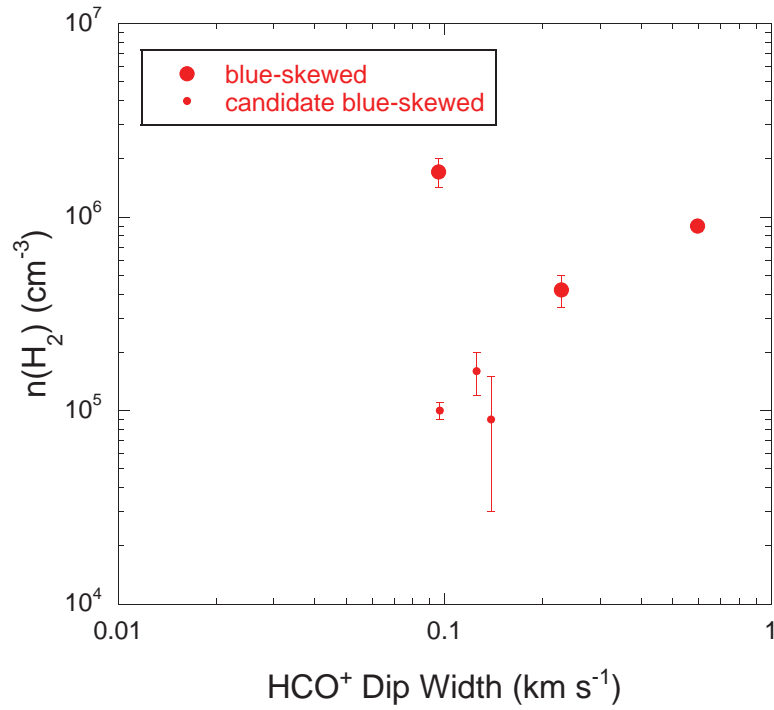


**Figure 16.** Core radius is plotted against the  $\text{HCO}^+$  dip width. The larger symbols represent the blue-skewed cores, while the smaller symbols the candidate blue-skewed cores.

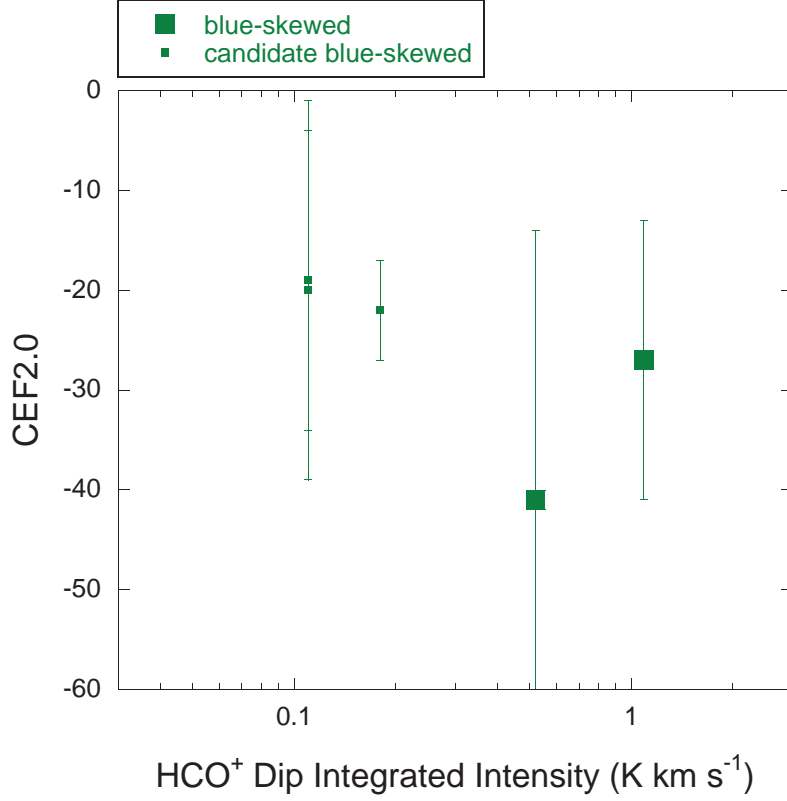


**Figure 17.** CEF2.0 is plotted against the HCO<sup>+</sup> dip integrated intensity.

of HCN and HCO<sup>+</sup>. Contreras et al. (2018) suggested that HCO<sup>+</sup> may be a better tracer of inward motions among other lines.

We have  $J = 3 \rightarrow 2$  data in hand for core 32. Tatematsu et al. (2020) pointed out a possibility that G211.16–19.33North3 (core 32) shows a hint of the blue-skewed line profile with a dip in the DCO<sup>+</sup>  $J = 3 \rightarrow 2$  emission with the ALMA ACA 7 m Array. The profile is the inverse P Cygni-like, because the ALMA ACA did not include the Total Power Array. Probably, the core is mostly resolved out with the 7 m Array, while part of emission from the core (center?) and foreground absorption of gas with inward motions have spatial distribution are resolved with it. In the current observations, we found that this core shows a candidate blue-skewed line profile with a dip in the HCO<sup>+</sup>  $J = 1 \rightarrow 0$  emission. The peak velocity of DCO<sup>+</sup>  $J = 3 \rightarrow 2$  coincides with that of the H<sup>13</sup>CO<sup>+</sup>  $J = 1 \rightarrow 0$  ( $v_{LSR} \sim 3.3$  km s<sup>-1</sup>). The velocity of the absorption dip in DCO<sup>+</sup>  $J = 3 \rightarrow 2$  is  $v_{LSR} = 3.65$  km s<sup>-1</sup>. Those of the first and secondary peaks of H<sup>13</sup>CO<sup>+</sup>  $J = 1 \rightarrow 0$  is  $v_{LSR} \sim 3.0$  km s<sup>-1</sup> and  $\sim 3.5$  km s<sup>-1</sup>, respectively. It seems that core structure with inward motions traced by DCO<sup>+</sup>  $J = 3 \rightarrow 2$  has larger velocity offset (0.3 – 0.4 km s<sup>-1</sup>) than that traced by HCO<sup>+</sup>  $J = 1 \rightarrow 0$  ( $\sim 0.2$  km s<sup>-1</sup>). If we take the largest velocity of the DCO<sup>+</sup>  $J = 3 \rightarrow 2$  dip at  $v_{LSR} = 3.9$  km s<sup>-1</sup> as we measured in the present study, the largest offset from the DCO<sup>+</sup>  $J = 3 \rightarrow 2$  peak emission is  $\sim 0.7$  km s<sup>-1</sup>. We wonder what these different velocity offsets mean. Different inward velocities at different radii may represent acceleration due to gravity. The “inside-out” collapse of Shu (1977) may have inward velocities of 0.2 and 0.6 km s<sup>-1</sup> at radii of  $3 \times 10^{16}$  and  $10^{16}$  cm (or 0.01 and 0.003 pc), respectively (Figure 2 of Zhou (1992)). Then, the different velocity offsets between the observations with the ALMA ACA and Nobeyama 45 m telescope may imply gravitational acceleration of the collapse. Using two independent observations, core 32 (G211.16–19.33North3) might show better evidence of inward motions.

#### 4.3. Comparison with Yi et al. (2021)

We compare  $\delta V$  of Yi et al. (2021) with a spatial resolution of 30'' with that in the present study with a resolution of 18''. There are 21 overlapping cores between their cores with  $\delta V$  estimate and this study. Their  $\delta V$  of the 21 cores have a mean of  $-0.1 \pm 0.3$  and a median of 0.0, whose absolute values are much smaller than the present study

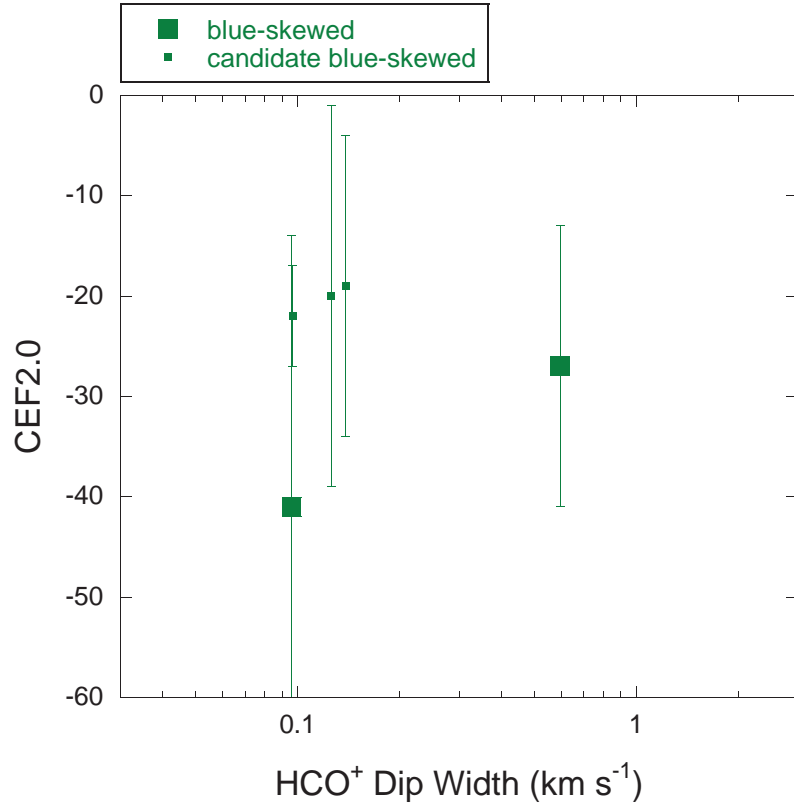


**Figure 18.** CEF2.0 is plotted against the HCO<sup>+</sup> dip width.

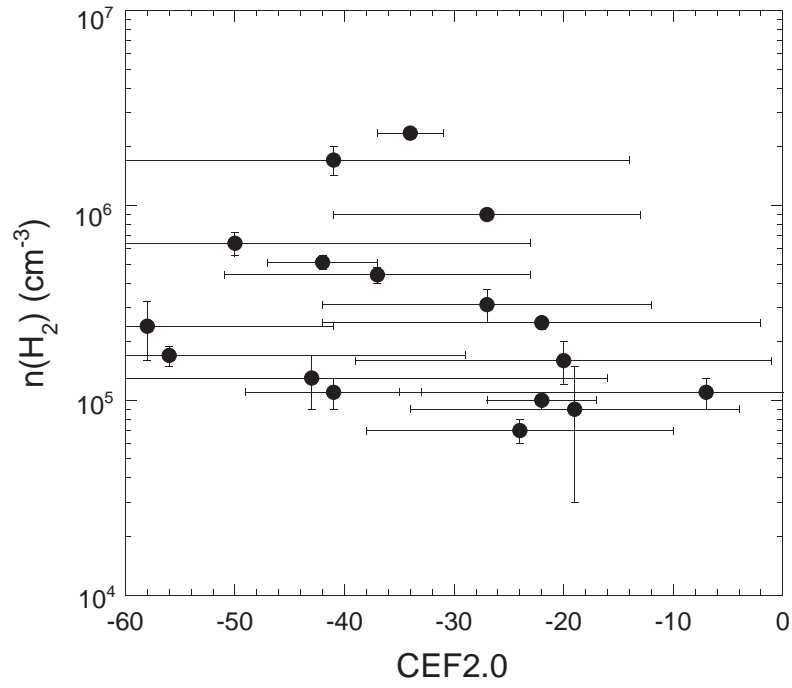


**Figure 19.** Core density is plotted against CEF2.0.

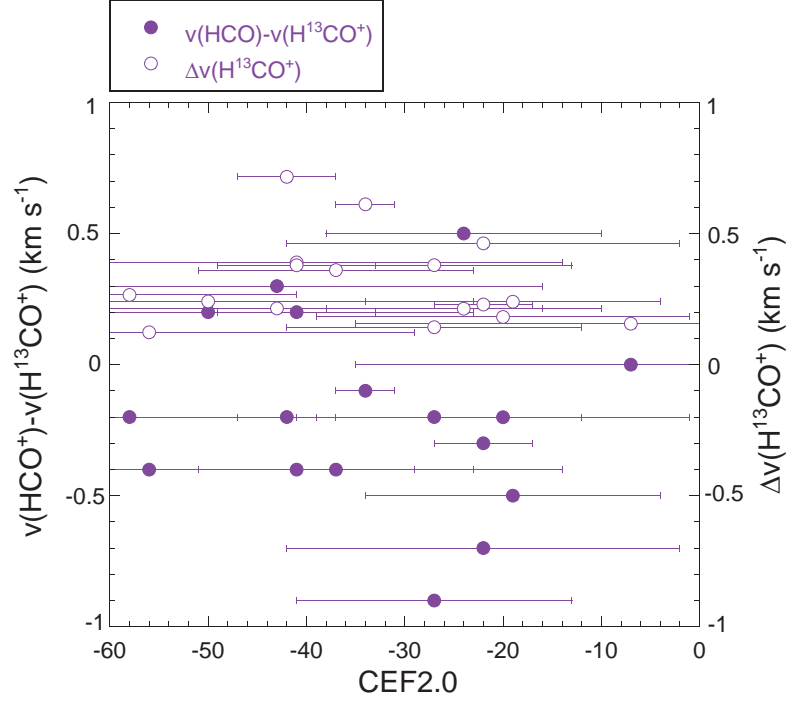


**Figure 20.** The velocity difference between  $\text{HCO}^+$  and  $\text{H}^{13}\text{CO}^+$  and the  $\text{H}^{13}\text{CO}^+$  line width are plotted against CEF2.0.

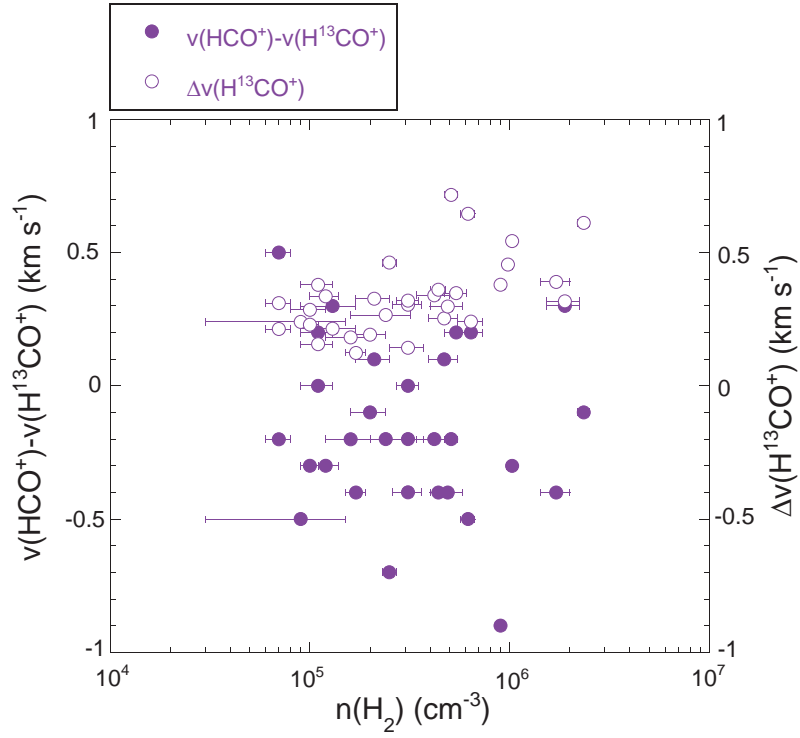


**Figure 21.** The velocity difference between  $\text{HCO}^+$  and  $\text{H}^{13}\text{CO}^+$ , and the  $\text{H}^{13}\text{CO}^+$  line width are plotted against density.



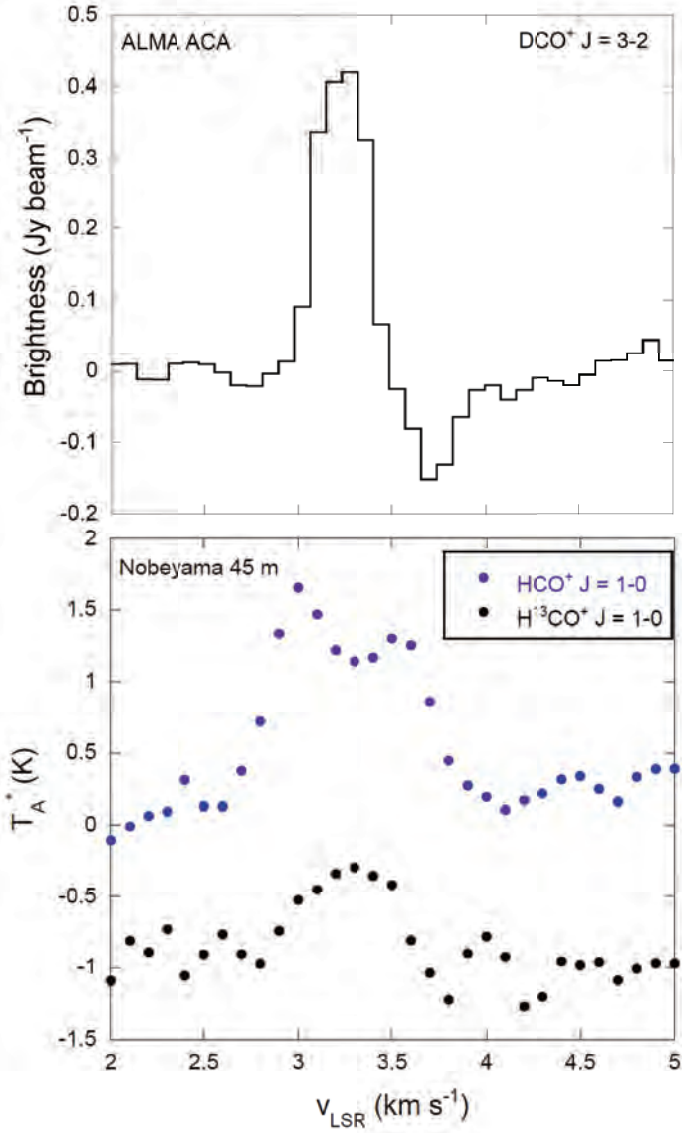


**Figure 22.** Comparison of the spectra in  $\text{DCO}^+ J = 3 \rightarrow 2$  observed with the ALMA ACA,  $\text{HCO}^+ J = 1 \rightarrow 0$  and  $\text{H}^{13}\text{CO}^+ J = 1 \rightarrow 0$  observed with the Nobeyama 45 m telescope, toward core 32 (G211.16–19.33North3).

(mean =  $-0.5 \pm 1.1$ , median =  $-0.6$ ). The main reason is that their  $\text{H}^{13}\text{CO}^+$  linewidths (mean =  $0.85 \pm 0.35 \text{ km s}^{-1}$ , median =  $0.83 \text{ km s}^{-1}$  for the overlapping 21 cores) are three (or more precisely  $2.72 \pm 0.55$ ) times larger than that in the present study (mean =  $0.33 \pm 0.14 \text{ km s}^{-1}$ , median =  $0.31 \text{ km s}^{-1}$ ). We believe that different spatial resolutions are one of the main reasons. Figure 23 compares  $\delta V$  with them and that in the present study. Correlation is rather poor.

Measurements of peak velocities are rather straight forward. The velocity differences between  $v(\text{HCO}^+) - v(\text{H}^{13}\text{CO}^+)$ ,  $v(\text{HCO}^+) - v(\text{N}_2\text{H}^+)$ , and  $v(\text{HNC}) - v(\text{HN}^{13}\text{C})$  6 are rather consistent. Then, we judge that the S/N ratio will not affect measurements of velocity differences so much. Probably, differences between beam sizes led to different statistics, which may represent complicated nature of motions near cores.

#### 4.4. Association with Filaments

Tatematsu et al. (2021) investigated whether the core properties such as radius, velocity dispersion, core mass, and virial parameter differ between the cores associated with filaments or those not associated, but they found no clear differences. We investigate hints of flows using statistics between them. We investigate association with filaments

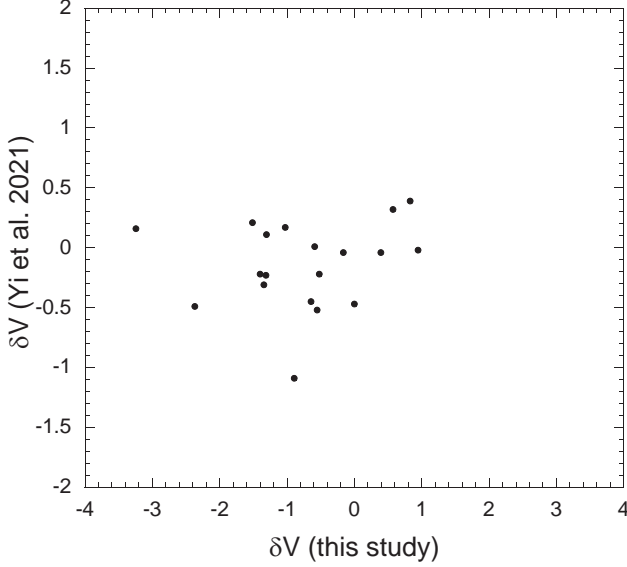


**Figure 23.** Asymmetry parameter of the 21 SCUBA-2 cores in Orion by Yi et al. (2021) is compared with that of the present study.

using the SCUBA-2 maps of Yi et al. (2018) by eye. Table 7 summarizes association with filaments. 20 out of the 30 starless cores (66%) are associated with filaments. We found that five (except for core 10) out of the six cores (71%) showing the blue-skewed or candidate blue-skewed profiles are associated with filaments. The current result does not suggest any outstanding statistics regarding the percentage of filament association in the cores showing blue-skewed or candidate blue-skewed line profiles with dips.

It is not easy to relate the filament dynamics and the cores showing blue-skewed or candidate blue-skewed line profiles with dips. Figure 24 to 26 show moment 1 (intensity-weighted velocity) maps toward the three cores with a hint of the velocity gradient along the filament.

One outstanding example is the filament connecting cores 17 and 18 (Figures 24 and 25, respectively), which clearly shows a velocity gradient along the north-south filament. If we can assume that this velocity gradient represents flows, these cores showing the candidate blue-skewed line profiles with dips may accrete the material along the filament. Another example is core 32 (Figure 26). See also the  $\text{N}_2\text{H}^+$  moment 1 map in Figure 18 of Tatematsu et al. (2021) containing the same core. This may represent an east-west velocity gradient, but the velocity field is complicated.

#### 4.5. Mass Rates of Inward Motions

We try to assess the mass rate of inward motions or flows. If we assume the Shu collapse in a core, the infall rate can be described as  $a^3/G$  (Shu 1977; Stahler et al. 1980), where  $G$  is the gravitational constant and  $a$  is the effective sound speed. We adopt the total line width (Fuller & Myers 1992) to obtain the effective sound speed  $a$  by assuming a kinetic temperature of  $T_k = 10$  K;

$$\Delta v_{NT}^2 = \Delta v_{obs}^2 - (8 \ln 2)kT_k/m_{obs}, \quad (1)$$

$$\Delta v_{TOT}^2 = \Delta v_{NT}^2 + (8 \ln 2)kT_k/\mu, \quad (2)$$

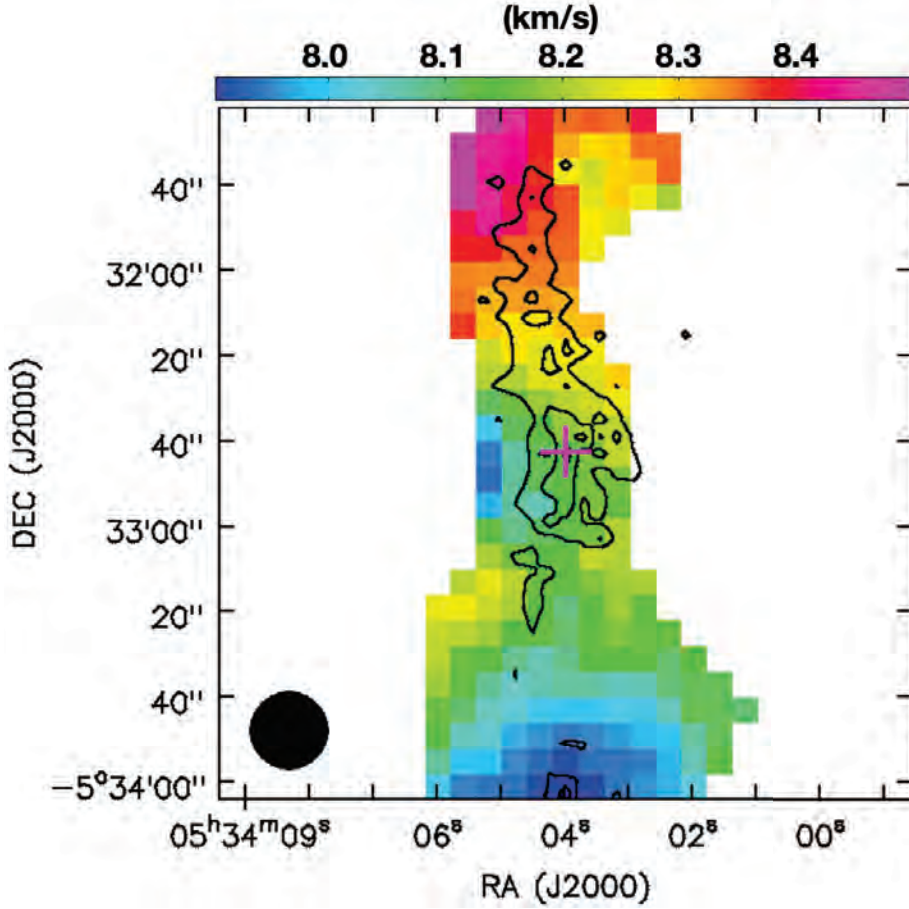


**Figure 24.** Gray-scale map of the moment 1 (intensity-weighted velocity) map of the  $\text{H}^{13}\text{CO}^+$  emission p toward core 17 (G209.05–19.73North). The plus sign represents the SCUBA-2 core center position. The circle in the bottom-left corner represents the half-power beam size ( $18''.2$  diameter). Contours of the SCUBA-2  $850\ \mu\text{m}$  continuum emission are drawn at levels of 50%, 70%, and 90% of the maximum intensity, which is  $259.3\ \text{mJy beam}^{-1}$ . This core is associated with a SCUBA-2 filament elongated in the north-south direction.

and

$$a = \sigma_{TOT} = \Delta v_{TOT} / \sqrt{8 \ln 2}, \quad (3)$$

where  $m_{obs}$  and  $\mu$  are the mass of the molecule used in the observations and the mean molecular mass per particle ( $2.33\ m_{\text{H}}$ ), respectively. The infall rate for the six (candidate) blue-skewed cores range from  $1.8 \times 10^{-6} M_{\odot}\ \text{yr}^{-1}$  to  $3.5 \times 10^{-6} M_{\odot}\ \text{yr}^{-1}$ . Second, we estimate another mass rate from the SCUBA-2 core radius and mass, and the effective sound speed above. We estimate the crossing time by dividing the radius by the effective sound speed, and then estimate the rate by dividing mass by the crossing time. Then, we obtain the rate to be  $(1.7 - 22) \times 10^{-6} M_{\odot}\ \text{yr}^{-1}$ . These two estimates ranges from  $2 \times 10^{-6} M_{\odot}\ \text{yr}^{-1}$  to  $2 \times 10^{-5} M_{\odot}\ \text{yr}^{-1}$ .

For the filament connecting cores 17 and 18, we estimate the possible flow rate along the filament, if we can assume the velocity gradient of the filament represents inflow. We estimate the LTE (local thermodynamic equilibrium) mass of the filament to be  $4\ M_{\odot}$  from the  $\text{H}^{13}\text{CO}^+$  data assuming an excitation temperature of  $\sim 5\ \text{K}$  and an  $\text{H}^{13}\text{CO}^+$  abundance of  $4.8 \times 10^{-11}$  (Ikeda et al. 2007, and references therein). The velocity gradient along the filament is  $\sim 1\ \text{km s}^{-1}\ \text{pc}^{-1}$ . We estimate a flow timescale of  $10^6\ \text{yr}$  from the velocity gradient, and then estimate the rate by dividing mass by the flow timescale. The inflow rate onto the core along the filament could be of order  $4 \times 10^{-6} M_{\odot}\ \text{yr}^{-1}$ .

These values may provide us the order of magnitude estimate of the rate for flows along filaments and inward motions toward the core center, if they exist.

## 5. SUMMARY

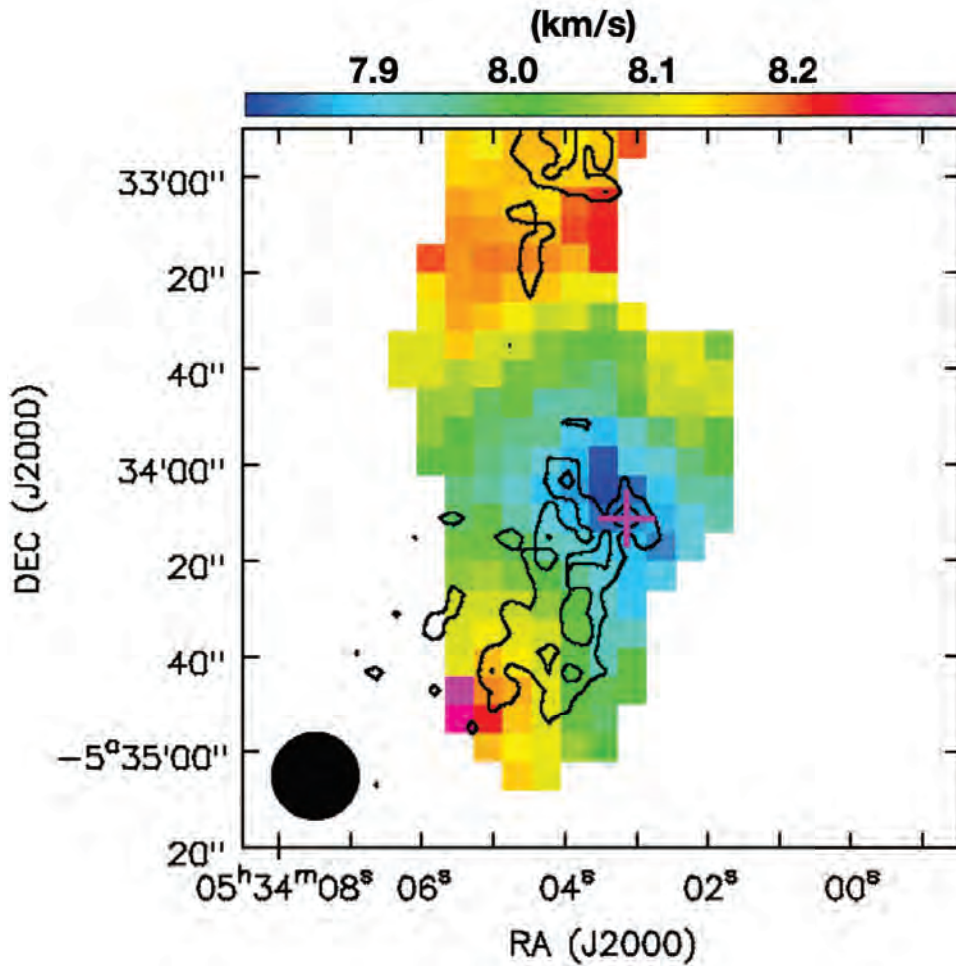


**Figure 25.** Same as Figure 24 but for core 18 (G209.05–19.73South). This core is associated with a SCUBA-2 filament oriented in the north-south direction. Note that this Figure is adjacent to Figure 24, and cores 17 and 18 are connected in the same north-south filament. The maximum intensity of the SCUBA-2 850  $\mu\text{m}$  emission is  $260.6 \text{ mJy beam}^{-1}$ .

We searched for inward motions toward the 36 SCUBA-2 cores (30 starless cores and 6 protostellar cores) in Orion. We used the Nobeyama 45 m radio telescope, and mapped them in the  $J = 1 \rightarrow 0$  transitions of  $\text{HCO}^+$ ,  $\text{H}^{13}\text{CO}^+$ ,  $\text{N}_2\text{H}^+$ ,  $\text{HNC}$ , and  $\text{HN}^{13}\text{C}$ . The asymmetry parameter (normalized velocity difference)  $\Delta V$ , which is the ratio of the velocity difference between  $\text{HCO}^+$  and  $\text{H}^{13}\text{CO}^+$  to the  $\text{H}^{13}\text{CO}^+$  line width is biased toward negative values, suggesting that inward motions are more dominant than outward motions. Three starless cores (10%) are found to have  $\text{HCO}^+$  blue-skewed line profiles, and another three candidate starless cores (10%) have blue-skewed line profiles. The peak velocity difference between  $\text{HCO}^+$  and  $\text{H}^{13}\text{CO}^+$  reaches  $0.9 \text{ km s}^{-1}$ , suggesting inward motions are supersonic at least partially. The mean of  $\Delta V$  of the six cores above was derived to be  $-1.4 \pm 0.7$ . All of them are found to be associated with cores with  $\text{H}^{13}\text{CO}^+$  emission. There is no clear indication that inward motions are observed predominantly at the latest stage in the starless phase. G211.16–19.33North3 also observed with the ALMA ACA in  $\text{DCO}^+ J = 3 \rightarrow 2$  shows blue-skewed features. The velocity offset of gas with inward motions in the ALMA ACA observations is larger than that in the Nobeyama 45 m telescope observations, which can be explained in terms of gravitational acceleration of inward motions.

## REFERENCES

- |  |  |
|--|--|
| <p>Aguti, E. D., Lada, C. J., Bergin, E. A., Alves, J. F., &amp; Birkinshaw, M. 2007, <i>ApJ</i>, 665, 457</p> <p>Aikawa Y., Ohashi, N., Inutsuka, S., Herbst, E., &amp; Takakuwa, S. 2001, <i>ApJ</i>, 552, 639</p> | <p>André, P., Di Francesco, J., Ward-Thompson, D., et al. 2014, in <i>Protostars and Planets VI</i>, 27</p> <p>Bergin, E. A.; Alves, J., Huard, T., &amp; Lada, C. J., <i>ApJ</i>, 570, L101</p> <p>Blitz, L., &amp; Thaddeus, P. 1980, <i>ApJ</i>, 241, 676</p> |
|--|--|

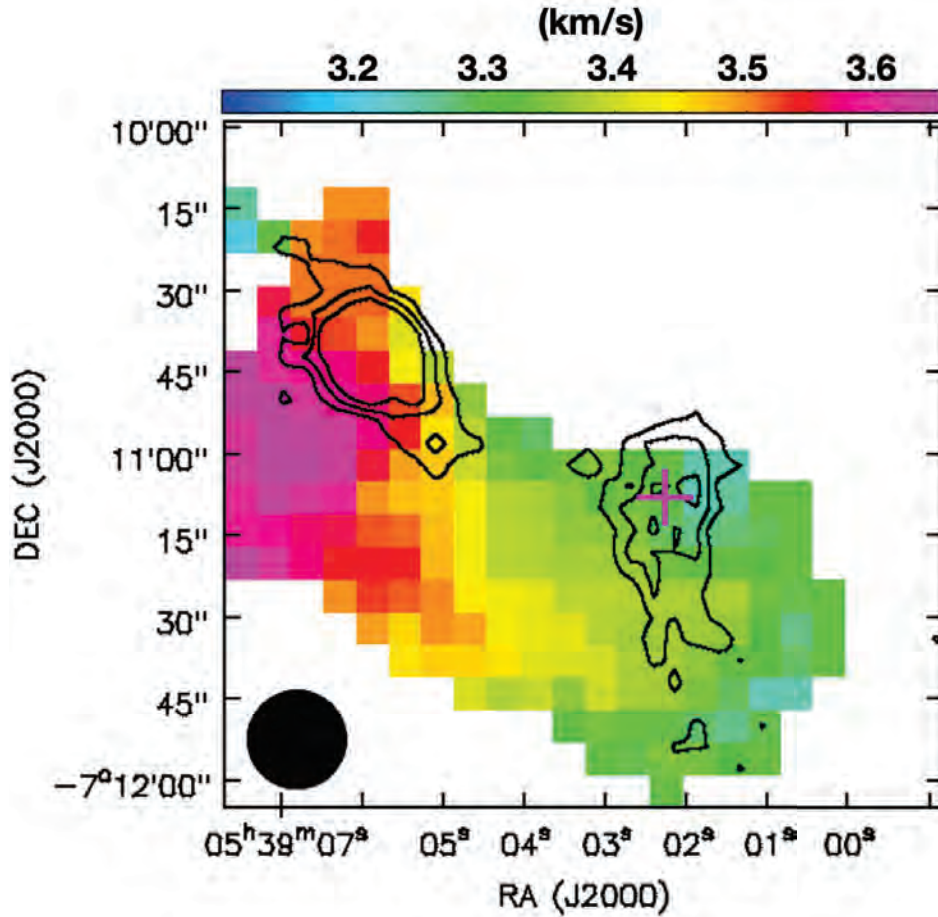


**Figure 26.** Same as Figure 24 but for core 32 (G211.16–19.33North3). This core is associated with a SCUBA-2 filament oriented in the east-west direction. The maximum intensity of the SCUBA-2 850  $\mu\text{m}$  emission is 83.9  $\text{mJy beam}^{-1}$ .

- 477 Caselli, P., Myers, P. C., & Thaddeus, P. 1995, *ApJ*, 455, 499  
478 L77 500  
479 Chen, M. C.-Y., Di Francesco, J., & Rosolowsky, E. 2020, 501  
480 *ApJ*, 891, 84 502  
481 Chira, R.-A., Smith, R. J., Klessen, R. S., Stutz, A. M., & 503  
482 Shetty, R. 2014, *MNRAS*, 444, 874 504  
483 Contreras, Y., Sanhueza, P., Jackson, J. M., et al. 2018, 505  
484 *ApJ*, 861, 14 506  
485 Crapsi, A., Caselli, P., Walmsley, C. M., et al. 2005, *ApJ*, 507  
486 619, 379 508  
487 Dutta, S., Lee, C.-F., Hirano, N., et al. 2020, *ApJS*, 251, 20 509  
488 Eden, D. J., Liu, T., Kim, K.-T., et al. 2019, *MNRAS*, 485, 510  
489 2895 511  
490 Emerson, D. T. & Graeve, R. 1988, *A&A*, 190, 353 512  
491 Emprechtinger, M., Caselli, P., Volgenau, N. H., Stutzki, J., 513  
492 & Wiedner, M. C. 2009, *A&A*, 493, 89 514  
493 Evans, N. J., II, *ARA&A*, 37, 311 515  
494 Evans, N. J., II, Rawlings, J. M. C., Shirley, Y. L. & 516  
495 Mundy, L. G. 2001, *ApJ*, 557, 193 517  
496 Evans, N. J., II, Di Francesco, J., Lee, J.-E., et al. 2015, 518  
497 *ApJ*, 814, 22 519  
498 Feng, S., Caselli, P., Wang, K., et al. 2019, *ApJ*, 883, 202 520  
521 Friesen, R. K., Medeiros, L., Schnee, S., et al. 2013, 522  
523 *MNRAS*, 883, 1513  
524 Fuller, G. A., & Myers, P. C. 1992, *ApJ*, 384, 523  
525 Fuller, G. A., Williams, S. J. & Sridharan, T. K. 2005, 526  
527 *A&A*, 442, 949  
528 Furlan, E., Fischer, W. J., Ali, B., et al. 2016, *ApJS*, 224, 5  
529 Getman, K. V., Feigelson, E. D., Kuhn, M. A., & Garmire, 530  
531 G. P. 2019, *MNRAS*, 487, 2977  
532 Gómez, G. C., Vazquez Semadeni, E., Shadmehri, M., & 533  
534 Ballesteros Paredes, J. 2007, *ApJ*, 669, 1042  
535 Gregersen E. M., Evans, N. J., II, Mardones, D., & Myers, 536  
537 P. C. 2000 *ApJ*, 533, 440  
538 Gregersen E. M., & Evans, N. J., II 2000 *ApJ*, 538, 260  
539 Hacar, A., & Tafalla, M. 2011, *A&A*, 533, 34  
540 Hirota, T., & Yamamoto, S. 2006, *ApJ*, 646, 258  
541 Ikeda, N., Sunada, K., & Kitamura, Y. 2007, *ApJ*, 665, 1194  
542 Jackson, J. M., Whitaker, J. S., Rathborne, J. M., et al. 543  
544 2019, *ApJ*, 870, 5  
545 Jeffries, R. D. 2007, *MNRAS*, 376, 1109  
546 Jessop, N. E., & Ward-Thompson, D. 2000, *MNRAS*, 311, 547  
548 63  
549 Kamazaki, T., Okumura, S. K., Chikada, Y., et al. 2012, 550  
551 *PASJ*, 64, 29



- Kerr, R., Kirk, H., Di Francesco, J., et al. 2017, *ApJ*, 874, 147
- Kim, G., Tatematsu, K., Liu, T., et al. 2020, *ApJS*, 249, 33
- Kirk, J. M., Ward-Thompson, D., & André, P. 2005, *MNRAS*, 360, 1506
- Könyves, V., André, P., Men'shchikov, A., et al. 2015, *A&A*, 584, A91
- Kounkel, M., Hartmann, L., Loinard, L., et al. 2017, *ApJ*, 834, 142
- Lada, C. J., Bergin, E. A., Alves, J. F., & Huard, T. L. 2003, *ApJ*, 586, 286
- Lee, C. W., Myers, P. C., & Tafalla, M. 1999, *ApJ*, 526, 788
- Lee, J.-E., Evans, N. J. I., Shirley, Y. L., & Tatematsu, K. 2003, *ApJ*, 583, 789
- Li, S., Lu, X., Zhang, Q., et al. 2017, *ApJ*, 912, L7
- Liu, T., Wu, Y., Mardones, D., et al. 2015, *Publications of the Korean Astronomical Society*, 30, 79
- Liu, T., Kim, K.-T., Juvela, M., et al. 2018, *ApJS*, 234, 28
- Loren, R. B. 1976, *ApJ*, 209, 466
- Lu, X., Zhang, Q., Liu, H. B., et al. 2018, *ApJ*, 855, 9
- Mardones, D., Myers, P. C., Tafalla, M., Wilner, D. J., Bachiller, R., & Garay, G. 1997, *ApJ*, 489, 719
- Minamidani, T., Nishimura, A., Miyamoto, Y., et al. 2016, *Millimeter, Submillimeter, and Far-Infrared Detectors and Instrumentation for Astronomy VIII*, 9914, 99141Z
- Olguin, F. A., Sanhueza, P., Guzmán, A. E. 2021, *ApJ*, 909, 199
- Padoan, P., Pan, L., Juvela, M., Haugbølle, T., & Nordlund, Å. 2020 *ApJ*, 900, 82
- Palmeirim, P.; André, P., Kirk, J., et al. 2013. *A&A*, 550, 38
- Perryman, M. A. C., Lindegren, L., Kovalevsky, J., et al. 1997, *A&A*, 323, L49
- Pickett, H. M., Poynter, R. L., Cohen, E. A., & and, M. D. S. 1998, *JQRST*, 60, 883
- Planck Collaboration, Ade, P. A. R., Aghanim, N., et al. 2011, *A&A*, 536, A23
- Planck Collaboration, Ade, P. A. R., Aghanim, N., et al. 2016, *A&A*, 594, A28
- Sahu, D., Liu, S.-Y., Liu, T., et al. 2021, *ApJ*, 907, L15
- Sandstrom, K. M., Peek, J. E. G., Bower, G. C., Bolatto, A. D. & Plambeck, R. L. 2007, *ApJ*, 667, 1161
- Sanhueza, P., Girart, J. M., Padovani, M. 2021, *ApJ*, 915, L10
- Sawada, T., Ikeda, N., Sunada, K., et al. 2008, *PASJ*, 60, 445
- Shirley, Y. L., Nordhaus, M. K., Grcevich, J. M., et al. 2005, *ApJ*, 632, 982
- Shirley, Y. L., *PASP*, 127, 299
- Shu, F. H. 1977, *ApJ*, 214, 488
- Stahler, S. W., Shu, F. H., & Taam, R. E. 1980, *ApJ*, 241, 637
- Tafalla, M., Mardones, D., Myers, P. C., et al. 1998, *ApJ*, 504, 900
- Tatematsu, K., Liu, T., Ohashi, S., et al. 2017, *ApJS*, 228, 12
- Tatematsu, K., Liu, T., Kim, G., et al. 2020, *ApJ*, 895, 119
- Tatematsu, K., Kim, G., Liu, T., et al. 2021, <https://arxiv.org/abs/2106.04052>
- Tokuda, K., Fujishiro, K., Tachihara, K., et al. 2020, *ApJ*, 899, 10
- van Moorsel, G., Kemball, A., & Greisen, E. 1996 in *A. S. P. Conf. Ser. 101, Astronomical Data Analysis Software and Systems V*, ed. G. H. Jacoby & J. Barnes (San Francisco, CA: ASP), 37
- Velusamy, T., Peng, R., Li, D., Goldsmith, P. F., and Langer, W. D. 2008, *ApJ*, 688, 87
- Wang, Y., Evans, N. J., II, Zhou, S., & Clemens, D. P. 1995, *ApJ*, 454, 217
- Yi, H.-W., Lee, J.-E., Liu, T., et al. 2018, *ApJS*, 236, 51
- Yi, H.-W., Lee, J.-E., Kim, K.-T., et al. 2021, *ApJS*, 254, 14
- Zhou, S. 1992, *ApJ*, 394, 204
- Zhou, S., Evans, N. J., II, Wang, Y., Peng, R., & Lo, K. Y. 1994, *ApJ*, 433, 131

## ACKNOWLEDGMENTS

K.T. was supported by JSPS KAKENHI Grant Number 20H05645. P.S. was partially supported by a Grant-in-Aid for Scientific Research (KAKENHI Number 18H01259) of JSPS.

594 *Facilities:* No:45m

595 *Software:* AIPS ([van Moorsel et al. 1996](#)), NOSTAR ([Sawada et al. 2008](#))